A MICRORESONATOR-BASED LASER DOPPLER VELOCITY SENSOR FOR INTERPLANETARY ATMOSPHERIC RE-ENTRY

Approved by:

Dr. M. Volkan Ötügen
Senior Associate Dean of Engineering,
Southern Methodist University

Dr. Tindaro Ioppolo
Assistant Professor of Mechanical Engineering,
Southern Methodist University

Dr. David A. Willis
Associate Professor of Mechanical Engineering,
Southern Methodist University

Dr. Dominique Fourguette
Vice President of Research & Development,
Michigan Aerospace Corporation

A MICRORESONATOR-BASED LASER DOPPLER VELOCITY SENSOR FOR INTERPLANETARY ATMOSPHERIC RE-ENTRY

A Thesis Presented to the Graduate Faculty of the

Lyle School of Engineering

Southern Methodist University

in

Partial Fulfillment of the Requirements

for the degree of

Master of Science in Mechanical Engineering

with a

Major in Design and Dynamic Systems and Controls

by

Benjamin John Alexander Wise

B.S., Mathematics, Southern Methodist University
B.S., Mechanical Engineering, Southern Methodist University
B.S., Physics, Southern Methodist University

May 19, 2018

ACKNOWLEDGMENTS

To say that this work would not have been possible without the guidance and instruction of my advisor and mentor, Dr. Volkan Ötügen, would be a bitter understatement. Dr. Ötügen consistently offered encouragement and advice, throughout my time at the Micro-Sensor Lab and throughout the writing of this thesis, and pushed me to be a better, more thorough researcher. His drive and enthusiasm for knowledge and the advancement of science and technology is truly inspiring and is something I continually strive to try to emulate. I would also like to thank all of the members of the Department of Mechanical Engineering at SMU's Lyle School of Engineering, and, more specifically, Dr. Ioppolo and Dr. Willis, for their assistance, both in class and in the laboratory, and their encouragement and advice throughout the process of writing and defending this thesis, and, more generally, during my seven years at SMU. My lab mates here at the Micro-Sensor Lab, Mr. Elie R. Salameh and Mr. Jaime DaSilva, also have my utmost respect and thanks for all of their hard work and the stimulating discussions we have had in the lab over the last year. I want to also extend my sincere thanks to our collaborators, Dr. Fourguette at Michigan Aerospace Corporation and her colleagues, whose hard work made it not only possible, but worthwhile to pursue this research.

I relied on the endless support of my friends during all the difficult times and I cannot begin to thank you all enough, especially for making me laugh when things were difficult, and for keeping me sane. Finally, I cannot even begin to thank my family, Dr. Pia D. Vogel, Dr. John G. Wise, and Mr. Eric J. Wise, as well as my extended family, for their undying patience and encouragement. Mom, Dad, and Eric, without you as role models to keep me on track, and without the support you gave me over the years, none of this would have been remotely possible.

From the bottom of my heart, thank you all; I am forever in your debt.

Wise, Benjamin John Alexander B.S., Mathematics, Southern Methodist University
B.S., Mechanical Engineering, Southern Methodist University
B.S., Physics, Southern Methodist University

A Microresonator-Based
Laser Doppler Velocity Sensor
For Interplanetary Atmospheric Re-Entry

Advisor: Dr. M. Volkan Ötügen

Master of Science in Mechanical Engineering degree conferred May 19, 2018
Thesis completed April 18, 2018

In this thesis, a laser velocity sensor concept based on optical microresonators is presented and the application to spacecraft atmospheric entry is explored. The concept is based on the measurement of Doppler shift of back-scattered laser light. Specifically, the Doppler shift is detected by observing the whispering gallery optical modes (WGM) of a dielectric microresonator excited by the back scattered light from particulates and gas molecules. The microresonator replaces the typical Fabry-Perot interferometer and CCD camera system, thereby significantly reducing the size and weight of the overall detection system. This thesis presents proof-of-concept results for this measurement approach. The Doppler shift of a tunable narrow line laser scattered from the edge of a rotating disk is measured using a $\sim 500\mu m$ diameter silica sphere as a microresonator. Different coupling modes (fiber-based and free-space) are explored and different resonator tuning methods (piezo-modulated and wavelength-modulated) are discussed. Results indicate that such a detection scheme is possible, although improvements to signal processing may be required for measurements in a gas. An improved signal processing algorithm is introduced and discussed.

TABLE OF CONTENTS

LIST OF FIGURES

LIST OF SYMBOLS

d_{max}	Index of Global Maximum in a Cross-Correlation Vector
d_{null}	Index of Global Maximum in an Auto-Correlation Vector
$\hat{\boldsymbol{h}}$	Cross-Correlation Data Vector
$\boldsymbol{k_0}$	Incident Light Wave Vector
$\boldsymbol{k_s}$	Scattered Light Wave Vector
$\boldsymbol{k_s} - \boldsymbol{k_0}$	Bisector of Incident and Scattered Light Wave Vectors
l	Optical Mode Number of Resonator
m	Laser Wavelength Slope (in Time)
N	Number of Data Points in a Scan
n_0	Resonator Index of Refraction
Q	Quality Factor
R	Radius of Rotating Disk Target
r	Resonator Radius
t	Time
t_D	Time when a Doppler Shift Occurs
$\boldsymbol{V}$	Velocity Vector of Laser Target

$\boldsymbol{V_x}$	Measurable Component of Velocity Vector (in a Doppler based Sensor)
x_i	i-th Data Point in a Scan
α	Half-Angle between $\boldsymbol{k_0}$and $\boldsymbol{k_s}$
ΔS	Shift Magnitude between WGM Spectrum Vectors
$\Delta\lambda_{Doppler}$	Change in Wavelength due to Doppler Shift
$\delta\lambda$	Wavelength Bandwidth of Resonance
λ	Wavelength
λ_{Center}	Center Wavelength of Time Varying Signal
$\lambda_{Initial}$	Initial (non-Doppler-shifted) Wavelength
μ	Mean Value of a Scan
$\hat{\boldsymbol{\xi}}$	Shifted WGM Spectrum Data Vector
σ^2	Mean Square Variance of a Data Scan
$\hat{\boldsymbol{\chi}}$	WGM Spectrum Data Vector
Ω	Angular Velocity of Rotating Disk Target

This is dedicated to my parents, Dr. Pia D. Vogel and Dr. John G. Wise, who always encouraged me to reach for something greater, and to my brother, Mr. Eric J. Wise, who humored and encouraged my antics over the years and always had something thought provoking to add.

Chapter 1

INTRODUCTION

The main motivation of this velocity measurement concept is the need for accurate speed measurements during atmospheric entry of spacecraft. For example, during the entry, descent, and landing (EDL) phase of Mars Missions – or for that matter any atmospheric EDL – accurate information on vehicle velocity, altitude, and attitude are critical for the success of the EDL operation. Accurate velocity information, however, is also critical to a myriad applications in the day-to-day lives of modern humans, such as in commercial aviation. This thesis proposes the use of whispering gallery mode (WGM) based optical microresonators [22] as a possible replacement for the bulky and heavy Fabry-Perot interferometers common in a range of other direct optical airspeed sensors, such as LIDAR systems. The WGM resonators will allow the miniaturization and significant weight reduction of these systems to make them feasible for planetary exploration and other applications. This thesis aims to demonstrate, at the proof of concept level, that Doppler shift measurement with WGM based sensors is possible and can provide high resolution velocity information.

We begin the discussion of the present work by first describing the motivation for this research in Section 1.1. Then the current state-of-the-art in speed and velocity sensing and LIDAR technologies are discussed in Sections 1.2 and 1.3. An introduction of WGM-based microresonator sensing applications follows in Section 1.4. The theory and operation of the present velocity sensing concept are presented in Chapter 2. In Sections 2.1, 2.2, and 2.3 the proposed sensor design at the high level, then the whispering gallery mode phenomenon and how it is used for sensing, are discussed. Finally, a discussion of how the measurements of Doppler shifts are made is presented in 2.4. Both methodologies for, and proof of concept results from, various velocity sensing experiments are discussed in Chapters 3 and 4. A signal processing method is detailed in Chapter 5, which improves the capability of the sensor.

1.1. Motivation

The need for high resolution velocity information has been most recently demonstrated by the crash of the Schiaparelli module (Entry Demonstrator Module or EDM) of the European Space Agency's ExoMars 2016 Mission. The Schiaparelli crash was caused primarily by sensor failure and faulty logic in reconciling measurements between the Radar Doppler Altimeter (or RDA, which was operating nominally) and the Inertial Measurement Unit (or IMU, which had become saturated and was producing a faulty signal). [9] The total dependence of the lander on the IMU, for all but the terminal 106 seconds of the mission, and the lack of redundancy and error checking in the measurement — faulty measurements from the IMU continued to be used for the duration of the mission, even after the IMU saturation flag was raised — were critical design errors that led to the total loss of the EDM. [9]

With the increasing complexity of EDL operations, accurate and (near) real time measurements of a lander's airspeed during entry, descent, and landing, as well as altitude and attitude (measured by complementary instruments), increases the likelihood of mission successes, which, as demonstrated by the Schiaparelli module, can often hinge on the accuracy (and fault–free operation) of only one sensing instrument. While fully integrated and tested devices for direct optical measurement of airspeed are commercially available [25], many are too bulky and far too heavy to be feasible for planetary exploration and other high speed applications.

1.2. State-of-the-Art in Velocity Sensing

It is useful to analyze the current state of the art in speed and velocity sensing before diving into the finer points of WGM sensing technology, to demonstrate the need for this new velocity sensing concept. A short analysis of the current LIDAR technologies available on the market and those currently under development and demonstration, given in Section 1.3, will show the deficiencies of current LIDAR technologies and make the case for the WGM based velocity sensor.

While the state-of-the-art speed and velocity sensing in laboratory settings has advanced significantly over the past few decades (particularly with the advances in Laser Doppler Velocimetry and Particle Image Velocimetry), many commercially utilized systems, especially in the aeronautics sector, rely on one of a handful of decades old techniques. The newest major advancement in these techniques being the Global Navigation Satellite System (GNSS), specifically the U.S. Global Positioning System (GPS), which first launched in the window between February 1978 and November 1985, four decades before the publication of this thesis. [13] Other techniques include various Inertial Navigation Systems (INS) or Inertial Measurement Units (IMU), and celestial navigation, which all work via dead reckoning. The most common system for aircraft speed measurement remains the static-pitot system, which is used to determine, among other things, the altitude, vertical velocity (rate of climb), the airspeed, true-airspeed, and Mach number of most aircraft. [32] Each of these systems, while tried and true, exhibit several major shortcomings. These shortcomings are dependent on systems and applications, but often include the size, mass, and physical limitations of high precision versions of these systems (typical aircraft GPS receivers can be several kilograms or heavier, and there are the obvious limitations of systems outside of GPS range), the possibility for signal saturation and drift (as in the Schiaparelli crash), and the inconvenience and dramatic engineering cost of introducing a critical system directly into a flow (especially at high Mach numbers) as for the static-pitot system, just to name a few. For the current application, the need for a physically small and lightweight, noninvasive, yet highly accurate system for determining the velocity of a vehicle should be clear. Additional applications of this technology are numerous and vary from high Mach number military and commercial aviation to high altitude weather data sensing, to applications in the autonomous vehicle space, and in environments where standard GPS signals fail to provide accurate or real time information, due, for example, to Urban GPS Degradation.

1.3. Current LIDAR Technologies

One of the newest, and most exciting avenues of research in the velocimetry field has been the development of laser based sensors: Particle Image Velocimetry (PIV) and Laser Doppler Velocimetry (LDV), are two sub-classification of LIDAR, or **L**ight **I**maging **D**etection **A**nd **R**anging, which focus on the detection of the velocity of particles, fluids, or solids. These techniques have the distinct advantages of being non-invasive, such that a flow being measured is not altered; remote, measurements can be made at considerable distances; fast, real-time measurement is limited only by data processing and analysis units and the shutter speed of the imaging system; and can give point, sheet, or volumetric measurements depending on setup and application.

Optical velocimetry techniques are fairly similar in how they operate. PIV typically utilizes a pulsed laser system and one or multiple CCD or CMOS Digital Cameras (depending on whether 2D or 3D information is required) to image the locations of tracer particles in a flow field. By repeatedly imaging of the same flow field with multiples of laser pulses (at intervals in time such that the movement of the tracer particles is small) the displacement of the tracer particles can be determined. [7, 8] By knowing the time delay between laser pulses illuminating the particles in the flow (imaged on a camera), the velocity field can be determined.

LDV operates by a slightly different principle: Determination of the velocity is done by measuring the Doppler shift caused by the relative motion of a particle. As discussed in more detail in Section 2.4, when a particle, traveling with a relative velocity to the laser source and detector (generally stationary or moving together in LDV techniques) scatters light, that light acquires a Doppler shift with respect to the original laser wavelength. Doppler shifts of most objects are generally a very small fraction of the frequency or wavelength of the light used and are not generally directly measurable. However, by overlapping two beams at the same location, an interference (or, fringe) pattern can be formed over the measurement volume and a beat frequency, generated by the particle scattering light from both (slightly angled) laser beams, can be directly measured. [7] This technique of optical heterodyning, with significant knowledge of the geometry of the system, and some signal processing, allows for the determination of the velocity of the particle passing through the measurement volume.

Single-beam LDV techniques also exist, however, without using optical heterodyning in the measurement volume (thereby forming a fringe pattern), the detection of Doppler shifts is more difficult. Such detectors generally rely on the use of one of several different types of interferometers, such as the Fabry-Perot interferometer. With the use of these high precision devices, which are generally quite large and heavy at that required level of precision, the Doppler shift can be directly measured from the scattered light from a target, such as a small particle. The disadvantages of increasing the mass and weight of already large and heavy systems by using an interferometer is what makes these single beam devices much less common than their heterodyning counterparts.

While LDV and PIV, are powerful techniques for measuring velocity (and by integrating and differentiating, the position and acceleration) of fluids, and have a wide variety of applications, actual LDV or PIV devices are not as common in industrial settings as other sensors. [24] Major deficits of most commercial LDV or PIV devices are the requirement for very customized setups of the instrument for a given application [37] and the large size, often on the order of $1m^3$, of many systems. [24] Truax, et. al, discusses the challenge of customizing LDV systems for use in the control of rolling mill applications for sheet steel and aluminum production: While the application is the same, (knowledge of the exact velocities of rollers and the sheet product is necessary to control the tension in the sheet and therefore the quality of the final product) attempting to transfer this system between aluminum and steel sheet production is difficult given the difference in reflectivities of the two products and the subsequent difference in the Doppler signal strength. [37] Additional difficulties in this application include requirements for large depth of field and dynamic range; environmental factors such as steam and scale, that can interrupt the signal; and the need for high measurement accuracy. [37] This example is fairly narrow in terms of the application, however, the issues with such a system are representative of the factors that plague many LIDAR systems, including PIV and LDV. While attempting to tackle all of these deficiencies is beyond the scope of this thesis, improvements over several of them can be achieved with WGM-based sensors. The size and physical mass of the system are the primary challenge within the current scope, however, issues of dynamic range, high measurement accuracy, and signal drop-out are also high level concerns and are discussed in this thesis.

1.4. Previous Optical WGM Microresonator Applications

The presently proposed method is essentially a single beam LIDAR technique that uses a whispering gallery mode optical microresonator instead of a Fabry-Perot interferometer. Whispering gallery modes are the optical modes of circular cross-section dielectric optical resonators, such as spheres, cylinders, disks, or toroids. When the resonance condition (discussed in Section 2.2) of the resonator is met, light is stored in the resonator. Increased light stored in the resonator corresponds to a decrease, or dip, in light transmitted through the coupling optics, or a peak in scattering from the resonator. Monitoring of the transmitted or scattered light gives high quality information about either the wavelength of the light being coupled or the optical path length of the resonator. Depending on the application, changes in optical path length of the resonator are related to physical inputs (force, pressure, temperature, etc.) to the resonator cavity.

Whispering gallery mode-effect sensors can detect a broad array of mechanical inputs and are classified as a sub-category under the umbrella of opto-mechanical transducers. When combined with a field programmable gate array (FPGA) or other data analysis system, these sensor packages convert a wide range of physical stimuli to digital signals which can then be utilized for a broad range of applications. More information on the operation and theory of optical WGM cavities and sensors will be discussed in Section 2.2 of this thesis.

High optical quality factor, Q, dielectric microresonators have received significant attention for their potential application in a wide range of fields. WGM applications have been explored in communication (switching, filtering, and multiplexing) and sensor technologies [23]. Sensors utilizing the whispering gallery mode (WGM) shifts of microspheres have been proposed for impurity detection in liquids, [15] mechanical sensing, including force, [16] pressure, [17] temperature, [12] and wall shear stress for aerodynamic applications, [4] as well as electric [14] and magnetic field strength measurement. [18, 19] The use of WGM microsensors has also been explored in the monitoring of structural health of composite materials. [28] Biological applications of WGM microsensors include the enhanced sensitivity of optical fluorescence biosensors to fluorophores; [5] the detection of unlabeled molecules, specifically proteins such as bovine serum albumin and streptavidin; and the ability to create a versatile, high sensitivity biological recognition elements capable of detecting specific analytes. [41] Additional unlabeled molecules such as single viruses, [3] single proteins, [2] DNA, and biological films [40] have also been detected in solution or their detection has been theorized by proof-of-concept experiments.

Another exciting application of optical WGM-based microresonators is as the sensing element in seismology applications. An optical WGM seismometer is shown below in Figure 1.1, and is the realization of US Patent No. 8,743,372. [10] One of the main demonstrated advantages of a WGM-based micro-sensor is the ability to measure a phenomenon with extreme resolution. Yet the sensors occupy an incredibly small space and subsequently have very low mass, as shown in Figure 1.1.

To date, however, conspicuously absent from the list of applications of WGM microresonators are the fields of velocity or speed sensing. To the author's knowledge, no velocity measurement concepts utilizing WGM microresonators have been explored at the time of publication, other than that published by the author. [42]

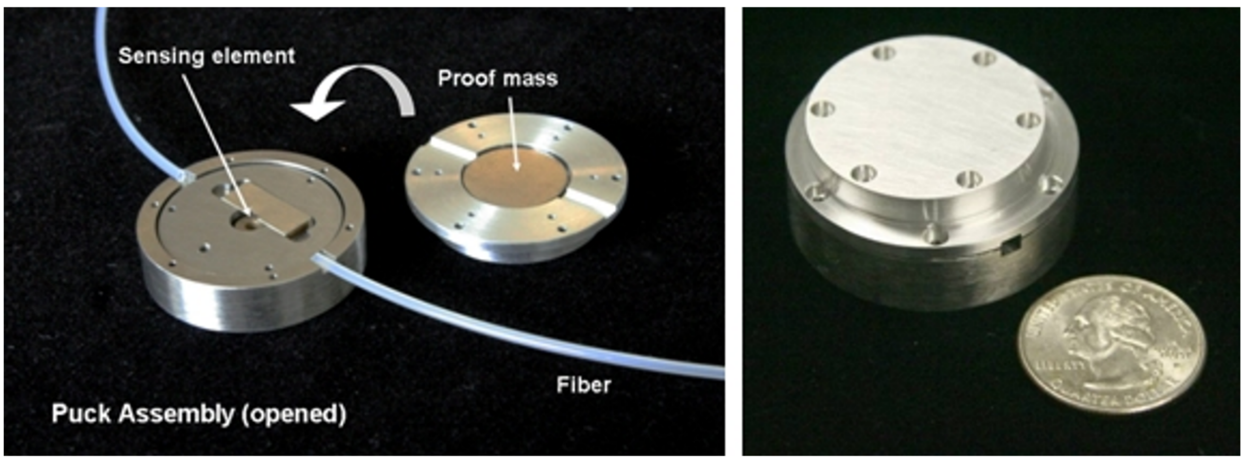

Figure 1.1. Comparison of the size of a sensing element from a Seismometer [31] with a US Quarter.

Chapter 2

MEASUREMENT PRINCIPLE

The most logical progression to introduce the measurement principle of this sensing system is to begin at the system level and then discuss the theory which drives the ability to make measurements, incrementally bringing the complexities into focus, until the overall function of the system is clear.

2.1. Proposed Sensor Package Design

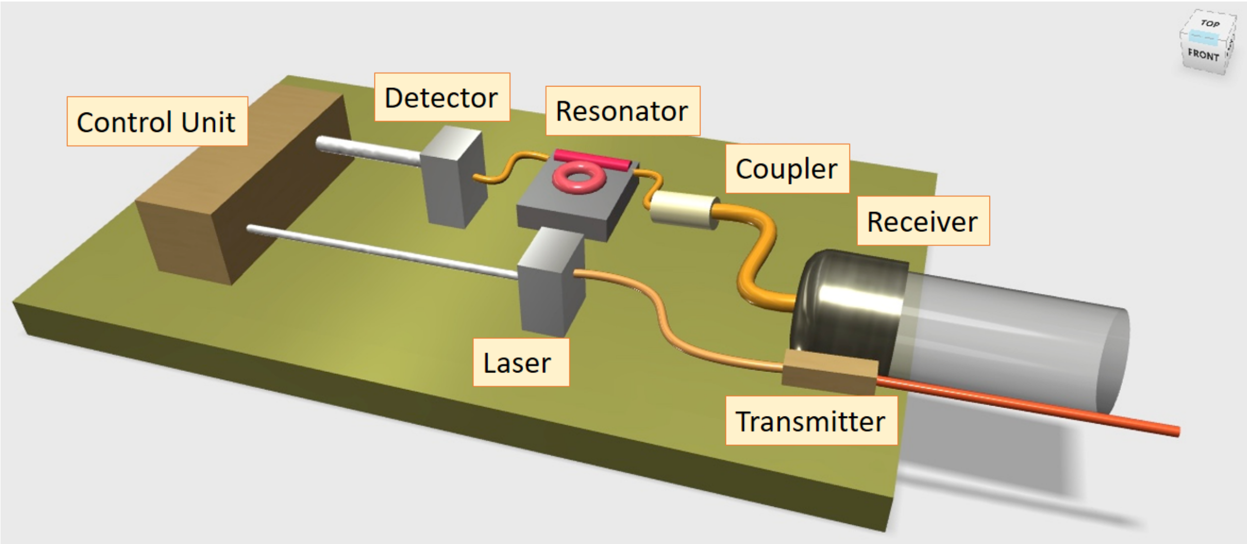

Figure 2.1. System Level Schematic of Velocity Sensor [31]

At the highest level, the components of a proposed system are shown in Figure 2.1. A preliminary design of the transmit/receive (TX/RX) telescope is shown in Figure 2.2. On the transmit side of the system are the control unit, which drives the laser, and the transmission optics (Parts E and I in Figure 2.2). The receiver side of the sensor system is more complex. It includes the receiving optics, shown in more detail in Figure 2.2; a mechanism for coupling the receive optics to the optical resonator; the resonator itself, which serves as the detection element; and finally a photo-detector, taking the form of a photo-diode or photo-multiplier tube. The analog output of the photo-detector is analyzed in the control unit.

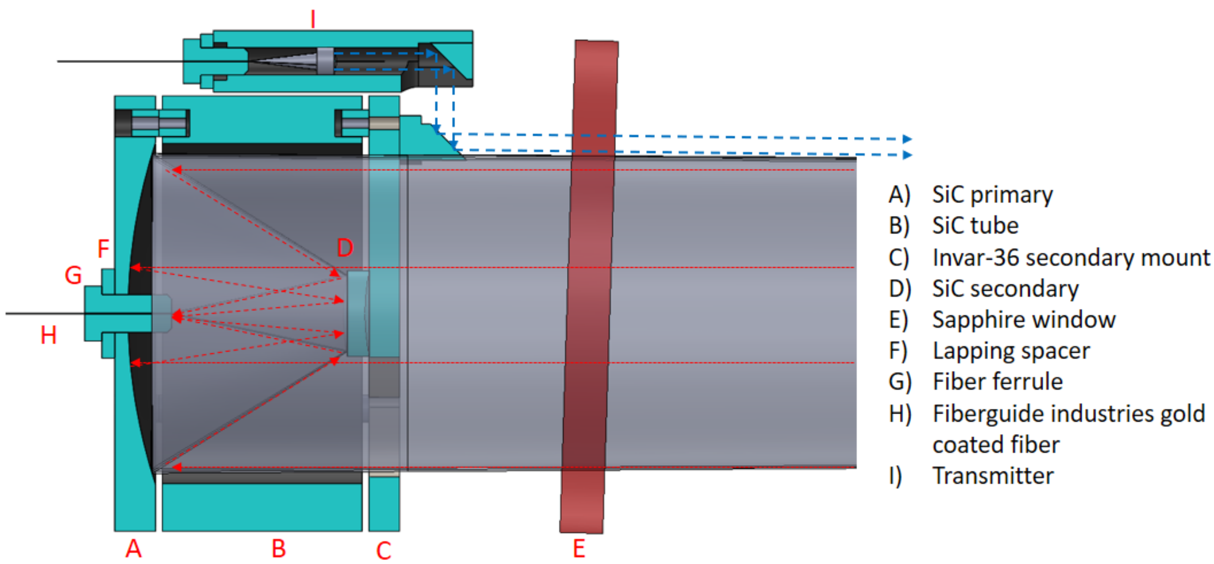

Figure 2.2. Preliminary Design of SPRY Transmit/Receive Telescope [31]

It is important to note the slight angle between the transmit and receive beam, which allows tight control of the interrogation volume and the distance to the interrogation volume. The sapphire window, Part E, allows for measurement during the entirety of the re-entry phase, including during phases with high atmospheric heating, while isolating the detector from heat and vibration. Preliminary designs include coupling received light into a fiber, as in Figure 2.2. However, free-space coupling of the resonator, by replacing Parts F-H with an assembly to hold the microresonator, is possible and may improve system performance, as explored in Chapter 4.

From a system point of view, the following functions are achieved: The control unit strictly controls the output of the laser operating in CW mode, which produces either a constant wavelength or a scanning (tuning) output; discussion of these two techniques is presented in Section 2.3. Drift and variance of the laser are controlled via calibration or a feedback loop. Light is transmitted through the TX/RX telescope. The wavelength of the transmitted light is Doppler shifted, due to the relative velocity between stagnant atmospheric particles and moving spacecraft. Doppler shifted light is back-scattered and collected by the receive (RX) telescope. Light is coupled from the receiver into a whispering gallery mode (WGM) optical cavity. The optical cavity is tuned via piezo-electric actuator or via tuning of the laser wavelength. Optical resonances are detected by the photo-detector and analyzed by the control unit.

2.2. Whispering Gallery Mode Phenomena

Figure 2.3. The Whispering Gallery at St. Paul's Cathedral in London [39]

Whispering gallery phenomenon was first explained in 1878, and mathematically described in 1910, by Lord Rayleigh, who encountered the phenomenon in sound at St. Paul's Cathedral in London, shown in Figure 2.3. [21] Lord Rayleigh observed that sound has a tendency to propagate along the surface of a concave shape and stay well confined along that path, such that only a small object placed in the path has the ability to intercept the wave. [21] This tendency of sound waves has a few very interesting properties: Firstly, the wave being confined to the surface of the shape means that little to no information is transmitted through the bulk of the volume of the concave cavity. Physically, this manifests as the inability to hear or measure the sound in locations other than near the edge of the cavity. Additionally, due to the confined nature of the sound, the propagation of a given sound is much further (and therefore the decay of sound is much smaller) than for a point source sound in open surroundings, which is governed by an inverse square relationship with the distance from the source.

These same phenomena can be observed in light in an optical resonator. The whispering gallery modes (also called morphology dependent resonances) discussed in this thesis are the optical modes of circular cross-section optical resonators, such as spheres, cylinders, disks, or toroids. When light from an extremely narrow linewidth source, such as a laser, is tangentially introduced into the cavity, as shown in Figure 2.4, it travels along the internal surface of the cavity (if the refractive index of the cavity material is larger than that of the surroundings). These optical cavities, such as the one shown in Figure 2.4, can be thought of as an arrangement of mirrors which form a standing wave of light. The cavity must be manufactured in such a way that the light remains well confined (as in an arrangement of mirrors), both in the direction of propagation and perpendicular to it. Light is then reflected internally with high efficiency (as long as the refractive index of the cavity is larger than that of the surrounding medium).

The measurement principle of a WGM-based microresonator is similar to that of a Fabry-Perot interferometer, with a few, mainly geometric, exceptions. One of the most immediate differences is the cavity shape. The WGM-based microresonators are circular in shape (rather than rectangular or confocal, as in Fabry-Perot interferometers, etalons, or Bragg gratings), and may be spherical, cylindrical, disk-shaped, or toroidal in nature. [22] The optical path must remain close to tangential — or more accurately, the optical path must make an angle larger than the critical angle (with respect to the surface normal) with the surface — in order to ensure that light in the cavity experiences total internal reflection and remains trapped inside the sphere.

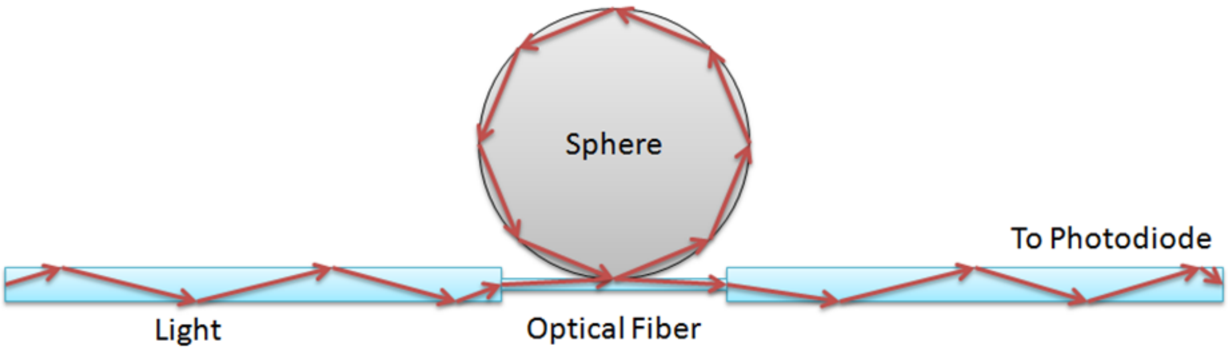

Figure 2.4. Schematic of a Fiber–Coupled WGM Microresonator

Light can be introduced into the dielectric cavity in various ways including via an optical fiber or prism coupler. Figure 2.4 shows, schematically, a typical fiber coupled WGM microresonator configuration. Laser light is coupled into the sphere through a thinned optical fiber (or another type of waveguide) at grazing angle. When the light returns to its entry point exactly in phase, an optical resonance is observed. To first order, the optical resonance condition is

$$2\pi r n_0 = l\lambda \tag{2.1}$$

which holds for $r >> \lambda$. An in depth analysis of the optical resonance condition can be found in Ioppolo, et al., [15], however, that level of detail is prohibitive for the present report. When the light from the laser is tuned across a narrow range, the optical WGM resonances are excited each time the condition of Equation 2.1 is balanced. Conversely, if the laser wavelength is held fixed and the radius, r, or the index of refraction, n_0, are varied, then optical resonances are also excited each time Equation 2.1 is met. The WGM resonances are observed as sharp dips in the transmission spectrum by a photodetector (such as a photomultiplier tube or photodiode, depending on light level) placed on the collection end of the fiber (as in Figure 2.4). Each dip in the transmission spectra corresponds to a different optical mode. Similarly, if the scattered light from the surface of the cavity is monitored using an optical detector, the WGM optical modes are observed as sharp peaks (see Figure 2.5).

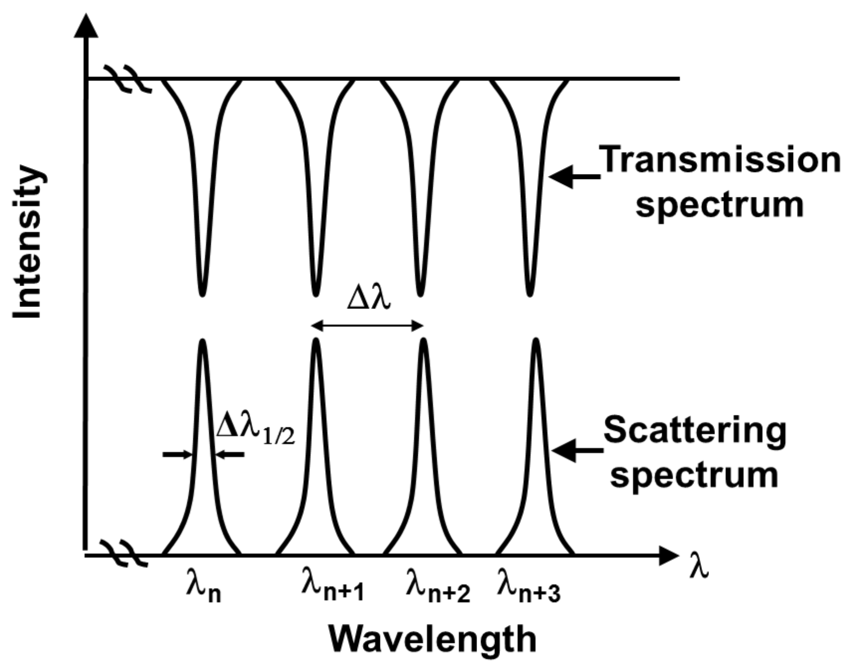

Figure 2.5. Idealized WGM Transmission and Scattering Spectra

While transmission and scattering spectra, similar to the ones shown in Figure 2.5, are achievable in a laboratory setting, they are neither simple to achieve, nor particularly useful in this application. The cross–correlation algorithm, as will be discussed in Section 5.1, actually produces stronger results for non-idealized WGM signals. Producing idealized WGM requires very strict control of a host of factors, including polarization of the light being coupled into the resonator (TE or TM only), highly regular curvature of the resonator, precise control of the launching angle of the light, etc. Intentionally coupling light with both TE and TM modes into, for example, a sphere at an angle such that the light is *not* launched into a perfectly equatorial orbit, results in non-idealized WGM spectra. The same phenomenon happens when the resonator is not a perfect sphere.

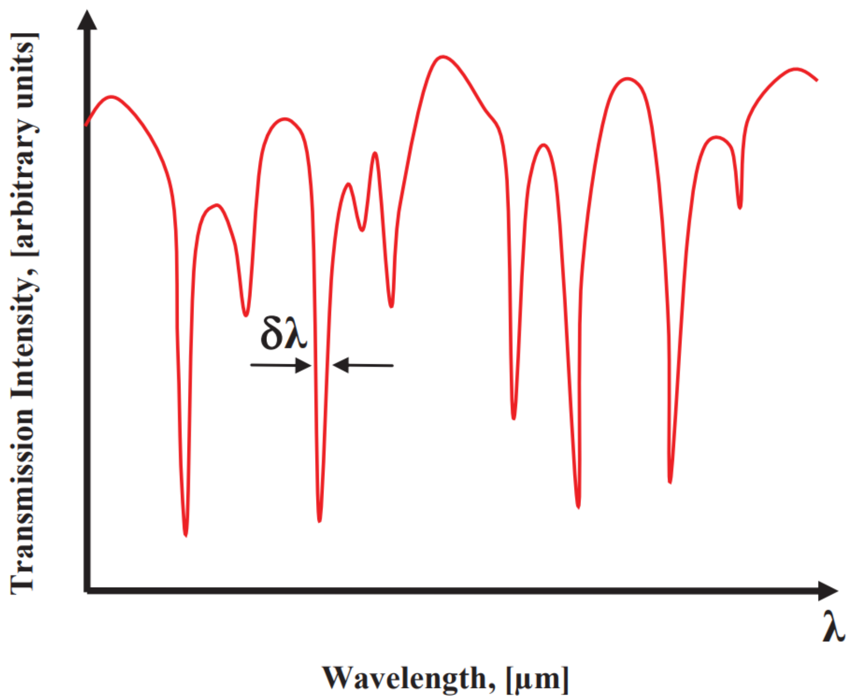

Figure 2.6. Non-Idealized WGM Transmission Spectrum [1]

Non-idealized spectra can be thought of as the superposition of a range of equatorial and azimuthal modes with varying TE and TM components. These non-idealized spectra are schematically depicted in Figure 2.6, with characteristic large relief and large numbers of features, and they increase the ability of the cross–correlation algorithm to detect small shifts in the spectra. Despite the non-ideal nature of the WGM spectra, the fact that light is coupled into the WGM microresonator tangentially and remains in the resonator via total internal reflection, rather than just the high reflectivity and/or anti-reflective coatings of, for example, a Fabry-Perot interferometer, means that the resonator itself has very low optical loss. Sources of this optical loss include surface imperfections and scattering, which can be minimized by a well-manufactured resonator and are the dominant source of loss, as well as minimal bulk absorption and quantum tunneling out of the resonator. [6]

The losses in a given resonator are described in terms of, Q, the optical quality factor, which is a ratio of energy stored in to the energy lost by a resonator, such that as losses vanish, $Q \to \infty$. The linewidth of the observed resonances, $\delta\lambda$ (Figure 2.6), directly impacts the measurement resolution (given that it is difficult to resolve any change in the signal much smaller than $\delta\lambda$). The Q-factor can be expressed as:

$$Q = \frac{\lambda}{\delta\lambda} \tag{2.2}$$

Unfortunately, the use of Equation 2.2 is imperfect, as the spectra are continuous and it is difficult to non-arbitrarily determine the edges of a whispering gallery mode, corresponding to $\delta\lambda$. For this reason, most definitions of quality factor for optical resonators use the full width at half maximum (FWHM) approximation for $\delta\lambda$. Using this approximation the quality factor can easily be determined from WGM spectra. A useful consequence of this definition of the quality factor is that it bounds the measurement resolution. For a given Q-factor optical resonator, the minimum shift in a given mode that can be reliably distinguished is, generally speaking, on the order of $\delta\lambda$. Without going into to much detail, and, assuming that each whispering gallery mode can be approximated by a Gaussian function, the FWHM interval is equal to just over $\pm 1\sigma$ resolution about the mean. While this relationship gives some bounds in the minimum measurement resolution for a single mode, a multitude of factors bound the actual measurement resolution on both sides. One such factor, which influences the upper bound, is the linewidth of the interrogation laser. As the laser linewidth becomes greater than $\delta\lambda$ it becomes difficult to impossible to determine, with the required accuracy, the location of a whispering gallery mode. However, the lower bound of resolution can also be improved by analyzing the shift in a multitude of modes, as will be described in Section 5.1.

The reason WGM microresonators in this configuration are so remarkable, and show so much promise for high resolution sensing, is the unusually high Q-factors they can achieve. In excess of $Q = 10^7$ is routinely achieved by our lab [16], with maximal values under closely controlled laboratory conditions of greater than 10^{11} having been achieved [30], and theoretical values predicted to be (for certain materials and wavelengths) in excess of 10^{15}. [11] All the while, the resonators maintain a remarkably small physical size and low mass. Therefore, they may be suitable for use in velocity sensing for planetary exploration missions.

2.3. Micro-Resonator Tuning

With a basic understanding of how whispering gallery modes work, their use in sensing is fairly simple to demonstrate. Equation 2.1 is key in understanding how measurements are made. As with most sensors, linear behavior over the measurement range is the ideal behavior and it is useful to start the analysis there. Rearranging Equation 2.1 in two different ways gives the two linear relationships that are most important in this thesis:

$$\lambda = [\frac{2\pi n_0}{l}]r \tag{2.3}$$

and

$$l = [2\pi r n_0]\frac{1}{\lambda} \tag{2.4}$$

Equations 2.3 and 2.4, are arranged such that there is clear relationship, in $y = ax$ form, between the two modalities in which resonators are tuned (in this thesis). Tuning, in this instance, describes the process of exciting specific optical resonances and observing them in order to in order to make a measurement. In this application, the parts of the equations that are in square brackets are considered to be constant. While this is not strictly true (n_0, r, and l being variable), in their respective modes of operation these variables are held constant or are analyzed for a given value, as is often the case for l. Furthermore, given the straightforward relationship between these variables and the output being measured (the left hand sides of the equations), they can easily be accounted for in a final sensor design via calibration.

Equation 2.3 describes the measurement modality for piezo-based tuning of the resonators, described in detail in Section 2.3.1. At its most basic, what occurs during this modality is the radius, r, of the sphere is varied in a predictable fashion in order to change the resonance wavelength of a given mode number, l, of the sphere. When used with a narrow linewidth laser and with proper calibration of the micro-resonator, it should then be possible to identify the exact wavelength of Doppler shifted light as the position of a given mode will shift proportionally to the Doppler shift of the interrogating light. When this wavelength is compared to the wavelength of the transmitted light, which must be known to high degree of accuracy, then calculation of velocity is straightforward.

In contrast, Equation 2.4 describes a modality of measurement in which the laser wavelength, λ, is varied over a range and several modes are excited. When the transmitted light is Doppler shifted and collected, the resonance modes will occur at slightly different wavelengths than before. Measuring the wavelength difference between the expected and actual for each mode will then give the Doppler shift between collected and transmitted light. In this way, WGM resonances can be used as an ultra-low-bandwidth notch-filter for measuring the Doppler shift, as described in more detail in Section 2.3.2.

Again, Equation 2.1 is a first order approximation and a more in depth discussion can be found in Ioppolo, et al. [15] However, in most applications, given the sensitive nature of resonator geometry and coupling conditions, most higher order effects can be accounted for with simple calibration or software compensation.

2.3.1. Piezo-Tuning of Micro-Resonators

It is useful to begin this section with some knowledge of the piezoelectric effect as it will elucidate why this process is described as *piezo-tuning*, rather than *displacement-tuning* or

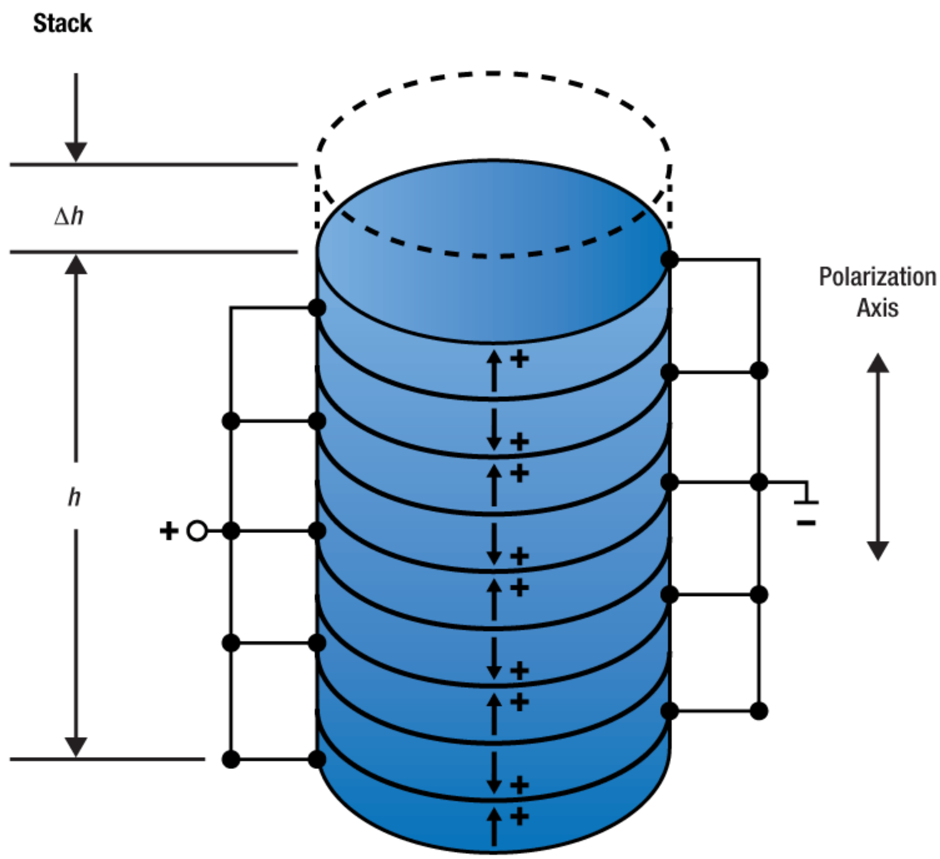

Figure 2.7. Piezo-Stack Schematic [36]

radius-tuning. The piezoelectric effect is the tendency of certain crystal lattices to accumulate a potential when they are compressed or elongated, or conversely, the tendency of a crystal lattice to elongate or shrink when placed under a high electric potential. As shown in Figure 2.7, when a number of crystal lattices are alternatively arranged between electrodes, a piezo-stack can be created. Varying the applied voltage between the electrodes will cause the expansion or contraction of the material. For scientific and industrial applications such as this one, piezo-stacks are often fitted with a strain gauge such that a feedback loop can be created. Closed-loop control of a piezo-stack with a strain gauge offers extremely high precision and controllable displacement that is at best inconvenient, and often impossible, to achieve by other means. Therefore, the use of *piezo-tuning* is, for all intents and purposes, synonymous with *displacement-tuning* or *radius-tuning*. The setup of such a system is shown in Section 3.2.1; by placing a microresonator between a piezo-stack and a fixed backstop, the radius of the microresonator can be varied with a high degree of control.

Figure 2.8 shows the process by which a piezo-tuning of resonances can be used to measure Doppler shifts. In Figure 2.8A, the laser wavelength is shown in the dashed red line and ramp waveform tuning of the microresonator radius, over time, is shown in blue. For convenience, the resonator radius is scaled by the constant factor in Equation 2.3, such that at times when the lines in Figure 2.8A intersect the resonator is in resonance. The (simplified and idealized) transmission spectrum corresponding to laser tuning in A is shown in Figure 2.8B. The sharp dips in B correspond to a resonance (mode) of the microresonator. If a Doppler shift occurs to the laser light at time t_D, as in C, and the sphere radius is tuned as in Figure 2.8D (blue), with the collected, shifted light in red, then the resonance spectrum in E results. Overlaid for clarity is the resonance dip (blue, dashed) from Figure 2.8B. Measuring the delay between the shifted resonance in green and the un-shifted resonance in blue, and with the knowledge of the function with which the radius is varied, determination of the Doppler shift over time is straightforward. Determining the relative velocity from the Doppler shift is simply a matter of geometry.

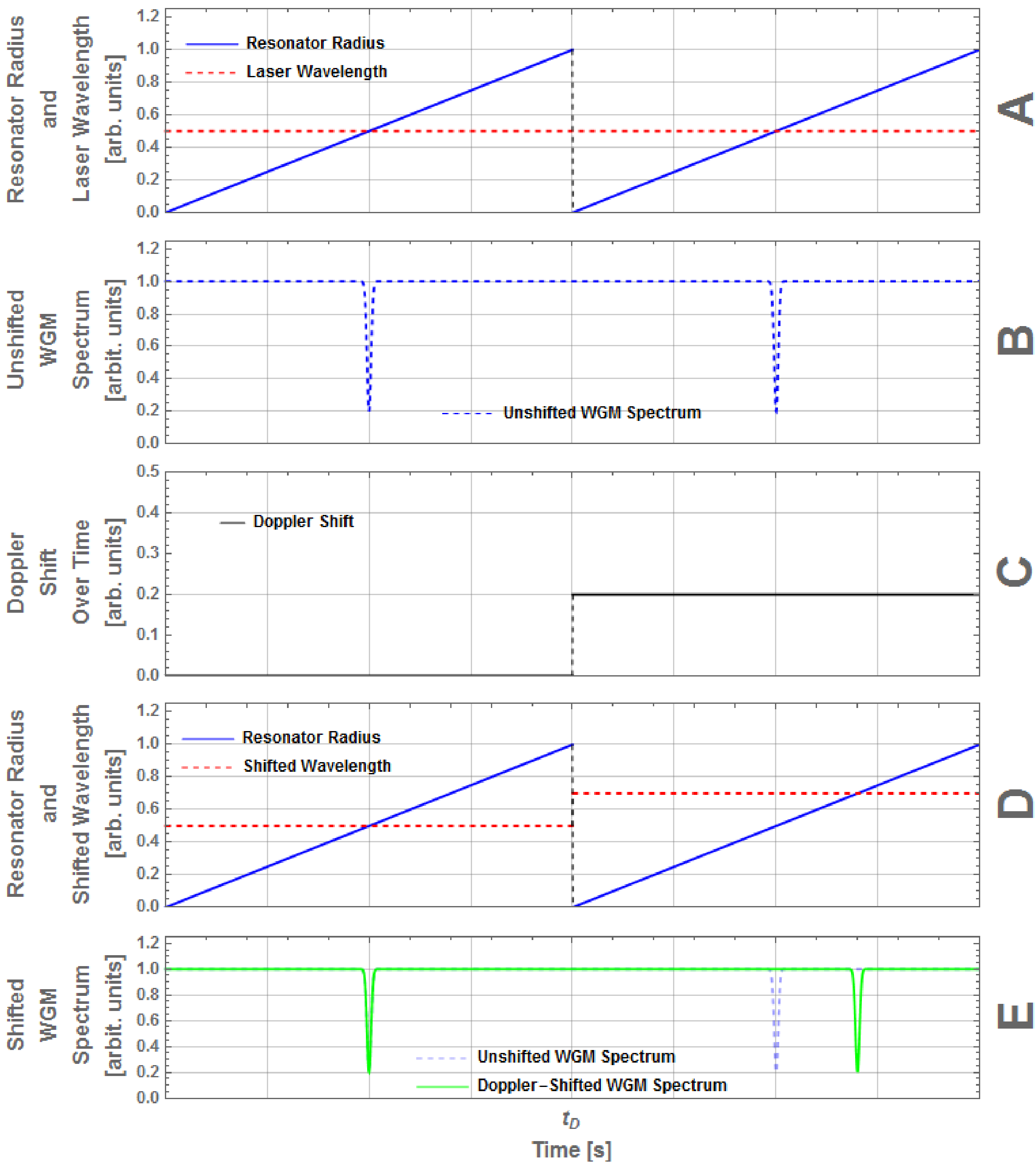

Figure 2.8. Idealized Piezo-Modulated WGM–Based Measurement of Doppler Shift

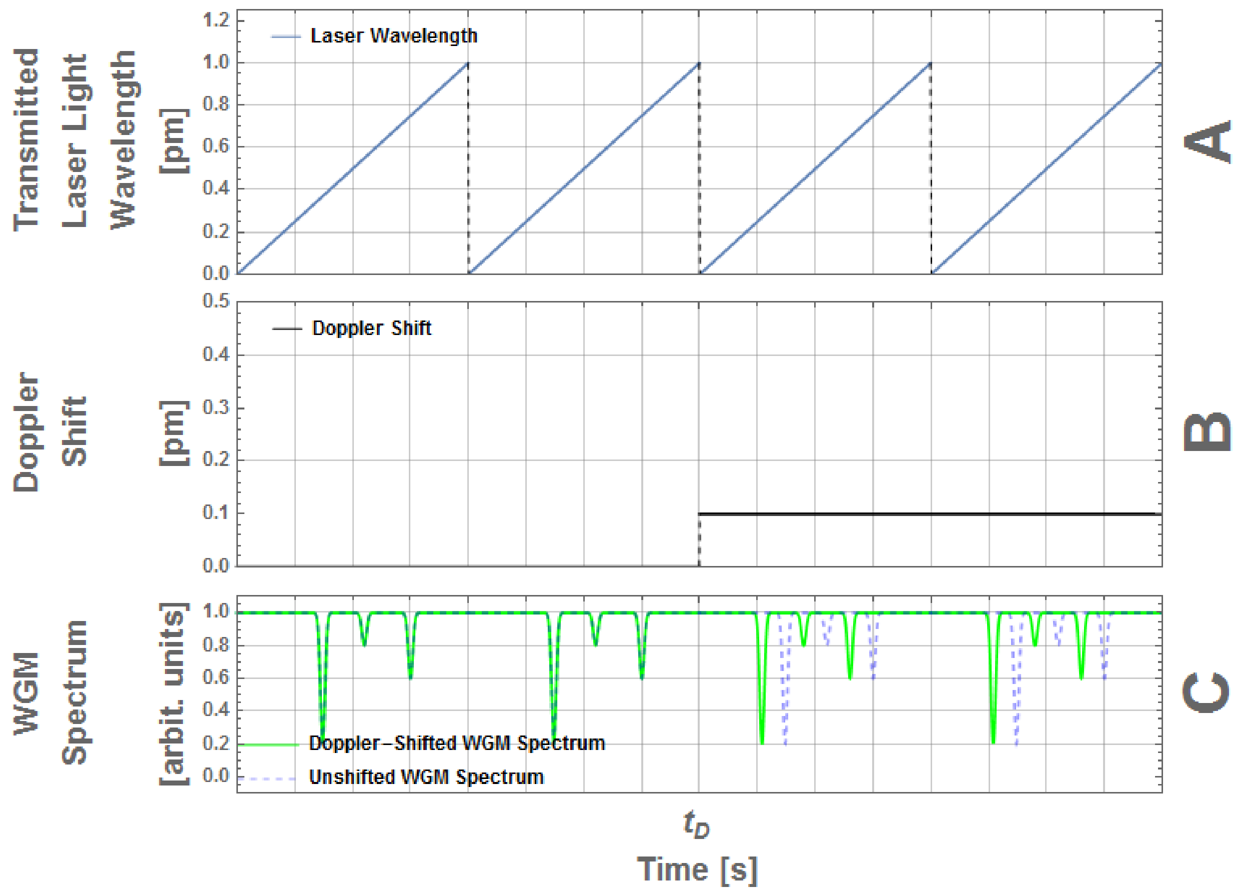

Figure 2.9. Idealized Laser-Modulated WGM–Based Measurement of Doppler Shift

In order to make a measurement of the WGM shift caused by the motion of the vehicle via laser-tuning, the scattering spectrum of some known reference signal must be compared to the scattering spectrum of a light signal containing the Doppler shift. The reference signal is recorded by measuring the WGM spectrum when the relative velocity is zero or can be analytically determined by knowing the exact wavelength response of the laser and the resonator. In order to generate a sweep of the WGM spectrum, the wavelength of the interrogation laser is varied. Figure 2.9A, shows a ramp waveform (approximated by $\lambda_{Initial}(t) = \lambda_{Center} + m \times t$, for a given repetition) about a central wavelength, λ_{Center}, (in present experiments $\sim 639nm$). This laser scanning, in combination with the various resonance modes of the resonator, leads to the initial resonance spectrum which is stored as the reference signal, shown in Figure 2.9C as the blue dashed line. This signal will remain constant as long as the wavelength of the light entering the resonator is *not* Doppler shifted. It is shown in Figure 2.9B and C that if the back-scattered light is Doppler shifted at time t_D by, say, an amount of $0.1pm$, a shift in the WGMs are observed.

With the knowledge of the reference signal (blue dashed line) the accurate detection of a shift in the wavelength can be determined by calculating the wavelength shift in the reference and scattering WGM spectra. In Figure 2.9C this corresponds to the time delay between the green (shifted) spectrum and the blue (reference) spectrum after the Doppler shift occurs in the second half of the plot. By measuring this delay between the features in the expected (known reference) signal and the unknown (measurement) signal, given the knowledge of the waveform of the interrogation laser (in this case, the slope of the laser wavelength in time, m), the shift in the wavelength occurring due to the Doppler effect can be determined without *a priori* knowledge of the Doppler shift. Clearly, if the measurement volume is an appreciable distance in away from the spacecraft and the laser wavelength is varied very quickly in time, the time delay of the round-trip path of the light will need to be subtracted. However, this time delay should be well known, given the angle of the transmission and collection optics and their respective fields of vision. Subsequently, determination of the velocity is a trivial matter of the geometry of the sensor and spacecraft.

2.4. Doppler Shift Measurement

In this application every experiment is a variation on a theme: a narrow line-width laser is directed at a target, the light is scattered (via a variety of targets) and collected, and subsequently, coupled (via free-space or fiber-coupling) into a microresonator, which is tuned by one of two tuning methods described above. Next, how light is scattered and how much Doppler shift is realized and measured is discussed.

In the proof-of-concept experiment in Section 3.2, it is demonstrated that it is possible to

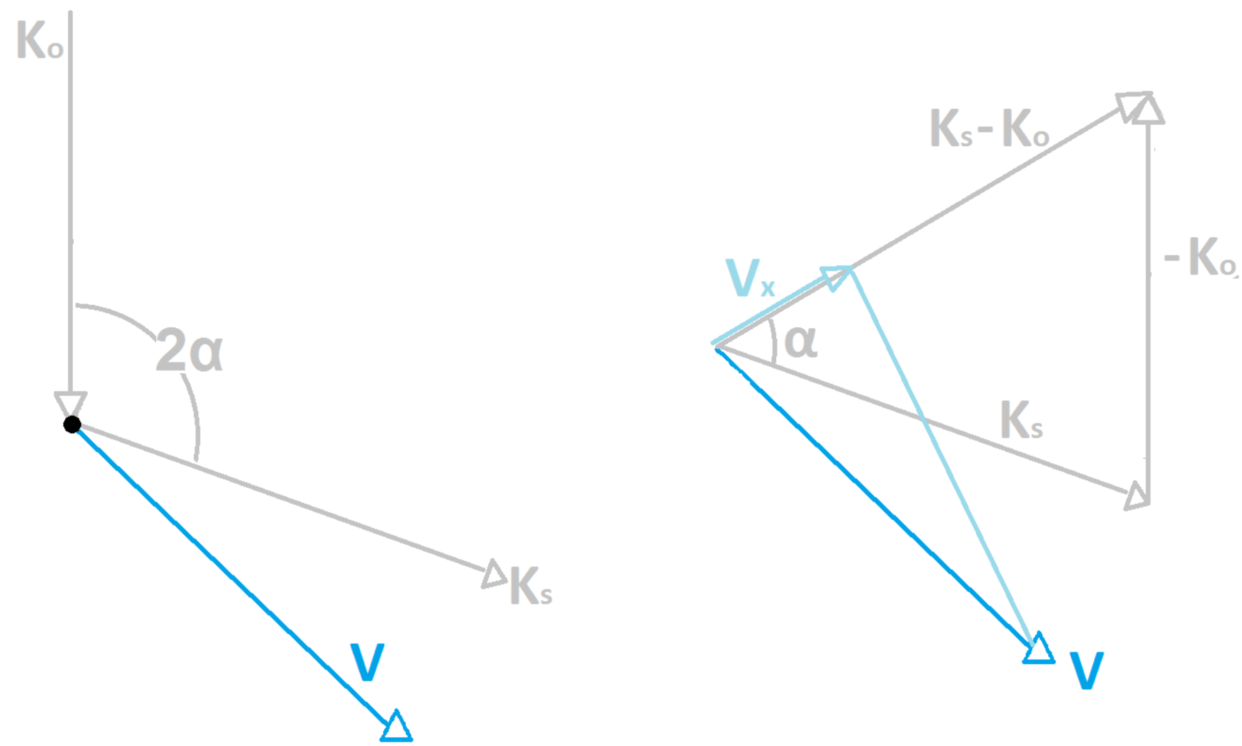

Figure 2.10. Vector Diagram of Doppler Shift Measurement from a Moving Target

make a velocity measurement from a moving solid target. The use of prefabricated, off-the-shelf, components for early stage experiments necessitated the use of a non-full back-scatter system. Given knowledge of the geometry of the system, shown in Figure 2.10, the frequency shift of light, Δf, was demonstrated by Ötügen, et. al. [29]

$$\Delta f = 2\frac{V_x}{\lambda}\sin(\alpha) \tag{2.5}$$

In Figure 2.10, $\boldsymbol{k_0}$ and $\boldsymbol{k_s}$ are the incident and scattered light wave vectors with respect to the moving target, $\boldsymbol{V}$ is the local velocity vector of the target, $\boldsymbol{\alpha}$ is the half-angle between $\boldsymbol{k_0}$ and $\boldsymbol{k_s}$, and, $\boldsymbol{V_x}$ is the measurable component of $\boldsymbol{V}$ projected along the vector $\boldsymbol{k_s} - \boldsymbol{k_0}$. Equation 2.5 governs the Doppler shift for any arrangement of transmission and collection beams and targets. Extrapolating this arrangement into the final use case for Mars missions, or, for atmospheric re-entry in general, and in the case of the proposed TX/RX system shown in Figure 2.2, the angle 2α between transmission and received signal is very small, maximizing the Doppler shift measurement along bisector of that angle. In this way, both the location and size of the measurement volume, determined by the overlap of the transmission light and the field of view of the telescope, and the attenuation of the signal along the bisector in the non-full backscatter configuration can be determined simply by varying the parameter α. Note that a precise measurement volume may not need to be defined, in this application, given the atmosphere is stagnant. In the final application, the scattering target will be suspended particles in atmosphere with high relative velocity between the stagnant atmosphere and fast moving spacecraft, so a full backscatter optical configuration may be convenient, but unnecessary, to make measurements.

The following chapters describe the process of building and improving these velocity sensors. Initially, experiments are carried out in order to determine the best option for tuning of the micro-resonators. Both piezo-modulated and laser-modulated tuning concepts are explored and are described in Chapter 3. After it is demonstrated that piezo-modulation requires very low signal repetition rates, the laser-modulation method is determined to be more likely to succeed, and used for the duration of the thesis. Subsequently, as a proof-of-concept, the rotational speed of a disk is measured using a low power, narrow line, tunable Littman-Metcalf cavity diode laser as the light source. [27] During this experiment, collected light is first coupled into a single mode optical fiber and then side–coupled into the microresonator in a similar fashion to that depicted in Figure 2.4. In a later experiment, simulated Doppler shifts are used to produce and artificially shift λ_{Center} by some amount $\Delta\lambda_{Doppler}$ via the laser controller, in order to determine the efficacy of free space coupling as compared to fiber coupling. Finally, a methodology for improving the signal via low-computational intensity signal processing is developed.

Chapter 3

FIBER-COUPLED RESONATOR EXPERIMENTS

3.1. Piezo-Modulated Resonance Excitation

During the earliest stage of this research the intended approach for the final design of the velocimeter was to utilize a laser with a narrow linewidth, and a fixed wavelength (rather than the narrow linewidth variable wavelength laser used presently). In order to compensate for the fixed wavelength of the microresonator we intended to utilize a piezo-stack to excite the optical modes of the resonator over a small range of wavelengths. By modulating the resonator in a controlled manner the Doppler shift due to a relative velocity can be determined by comparing the resonance wavelengths at a given speed to a known (ideally zero velocity) reference. Via calibration, the extension of the piezo actuator could be related to the deformation of the sphere and therefore to the shift in the resonance condition and subsequently the relative speed of the sensor.

3.1.1. Experiment

The general system setup is shown in Figure 3.1 in schematic form. The two function generators, shown in grey, supply the tuning signal to the piezo-stack controller and the laser. In the actual sensor, only one of these two components will be needed (the function generator controlling the piezo-stack) as the function generator controlling the laser will be replaced with the receive side of the SPRY telescope, shown in Figure 2.2. In this experiment, the laser and associated function generator serve to generate simulated Doppler shifts, which are measured by the remainder of the system. A ThorLabs 150V co-fired piezoelectric actuator with strain gauge (Part # PZS001) is used with a strain gauge pre-amp circuit (Part # AMP002) and a 1-channel 150V benchtop piezo controller (Part #BPC301) to tune the

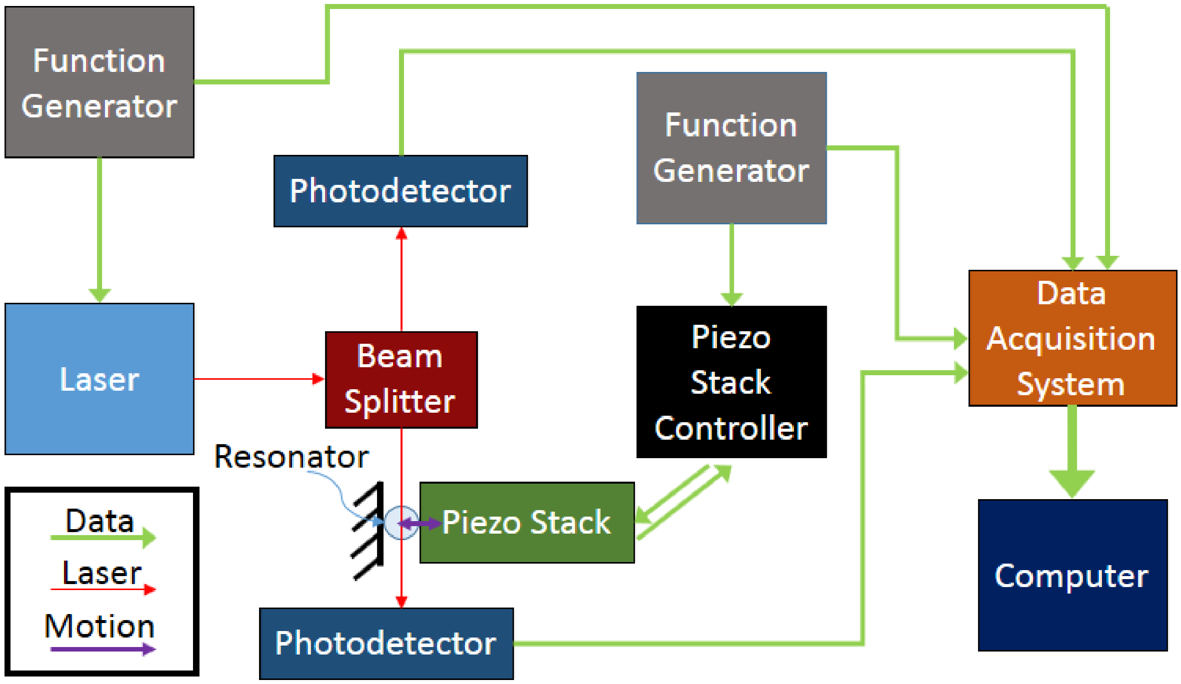

Figure 3.1. Piezo-Tuned Microresonator Setup Schematic

microresonator. [33, 34] The combination of these three devices forms the closed-loop system required for accurate displacement of the piezo-stack and, in conjunction with the function generator, allows repeated periodic tuning.

In Figure 3.1 the color of each arrow indicates the type of information that is transmitted between components. Green arrows represent the *data* flowing through the system. More specifically, these pathways are the electrical connections between components, for the most part, carrying analog signals. Red arrows represent *laser* signal, carried, via optical fiber between the various optical components. The single purple arrow represents the actual physical displacement of the piezo-stack acting on the microresonator. The directionality of the arrows shows whether each component is connected via open-loop or closed-loop to the subsequent component.

The $1.3\mu m$ laser light is produced by a Lucent telecom-band fiber-coupled laser diode (Part # A2334D7P) and controlled via ILX Lightwave LDC-3724C laser diode controller and ILX Lightwave LDM-4980 laser diode mount. The ILX Lightwave system allows for a high level of control of the laser wavelength by controlling both the temperature and current of the laser diode, giving high stability and very small laser linewidth. [1] The light is split via $90\% : 10\%$ beam splitter to a reference photodetector and via fiber-coupling to the microresonator and the signal photodetector (ThorLabs # PDA10CS). The reason the beam splitter and reference photodetector are included, as opposed to only using the signal photodetector, is to allow an *in-silico* removal of any change in laser power associated with tuning the laser diode. Unfortunately, many telecom lasers are current tuned lasers, meaning that in order to modulate the wavelength of the laser the actual power supplied to the diode is changed. As a result of this current-tuning of the laser, the photodetectors observe a change in power not related to the WGM resonance. With the help of a reference signal (containing no WGM resonances), the resultant intensity change can be removed as a part of the software signal processing accomplished on the desktop computer.

The data acquisition system used in this experiment is a National Instruments PXI-1033 5-slot integrated remote controller PXI chassis used with a NI PXI-6115 simultaneous sampling multifunction I/O module, which offers 4 analog input channels, with 12 bit resolution analog to digital converters and a sample rate of 10^6 samples/s, and a NI BNC-2110 shielded BNC connector block. [26] This system both discretizes and digitizes the data, which is fed to a desktop computer for signal collection and processing with software built in-house in the NI LabView graphical programming language.

Figure 3.2, shows a photograph of the piezo-tuned resonator, as well as some of the smaller components that are not shown in the system level diagram in Figure 3.1. These components, such as the two 3D translation stages and microscope (out of view, top of Figure 3.2) are crucial to attaining the precise relative positioning of the microresonator (fixed to the resonator backstop), the coupling fiber, and the piezo-stack. Also shown in this view are the relative size of the piezo-stack, the resonator, and the coupling fiber, further

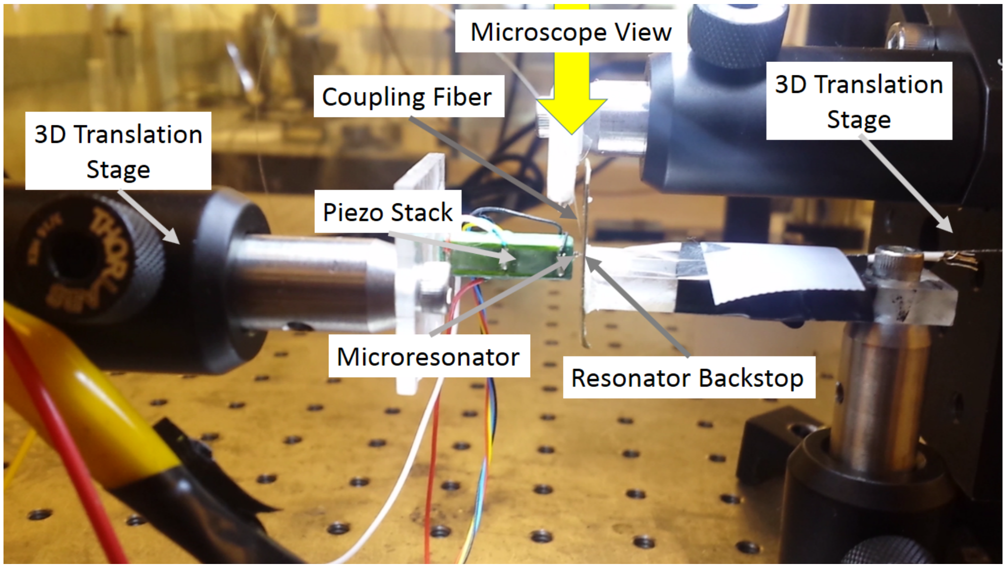

Figure 3.2. Piezo-Tuned Microresonator Experimental Setup

demonstrating the compactness of this system.

Figures 3.3 and 3.4 show a closeup view of the microresonator in the tuning configuration. The view in Figure 3.3 was taken with a digital camera on a microscope and shows a working view of the piezo-stack, resonator, backstop (on the right), and coupling fiber. It is noteworthy that while the microresonator was not in direct contact with the backstop in this case, the microsphere stem (made of optical fiber) has a much larger stiffness than the polydimethylsiloxane (PDMS) microresonator at these length scales, and acts as an effective backstop. The coupling optical fiber, highlighted in red, is barely visible in this view as it is slightly out of the focal plane of the microscope. In Figure 3.4, red, visible-wavelength light was introduced into the laser end of the fiber in order to better demonstrate sphere fiber-coupling. This picture shows a similar setup with the piezo-stack backed slightly away from the resonator for clarity.

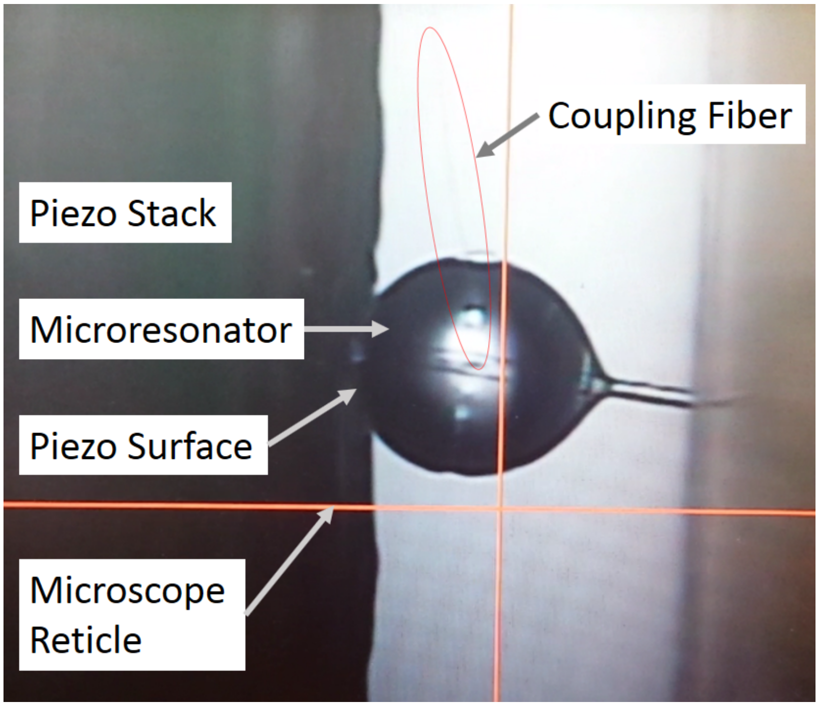

Figure 3.3. Microscope View of Piezo-Tuned Microresonator

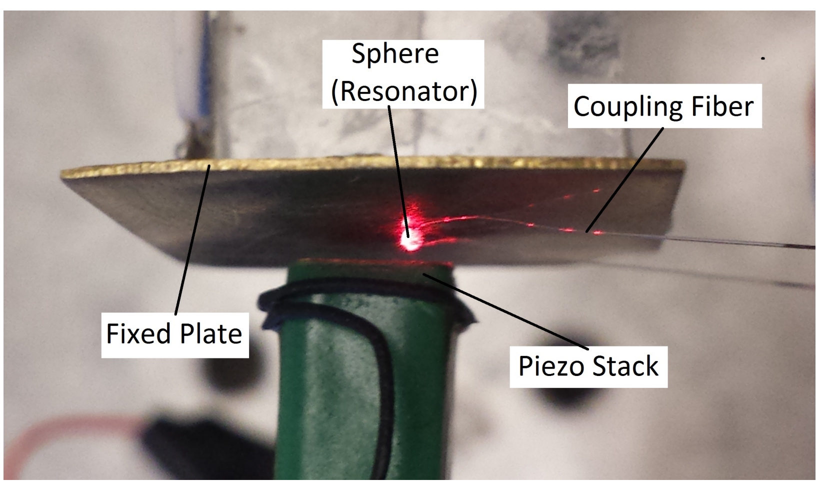

Figure 3.4. Piezo-Modulated Resonator (Piezo-Sphere distance increased for clarity.)

3.1.2. Results

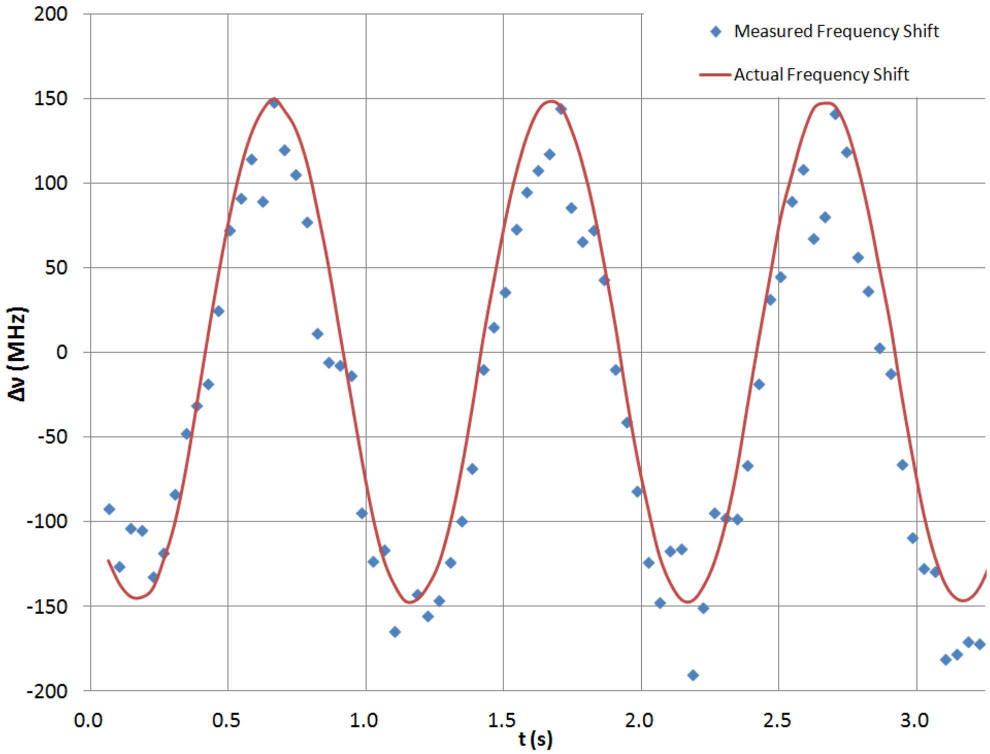

Figure 3.5. Measured vs. Induced (Actual) Doppler Shift

Figure 3.5 shows the actual laser frequency shift (simulated Doppler shift) and that measured by the resonator. It should be immediately clear from Figure 3.5, that at this level, the experiment to determine whether this sensing concept (fixed wavelength laser, piezo-tuned microresonator used for determination of Doppler shift) is possible. The Doppler shifts simulated in this experiment are fairly large, on the order of $\pm 150 MHz$. With a laser in the visible spectrum, this corresponds to a full-backscatter Doppler shift caused by motion in the $\pm 10^3 m/s$ range, which when cast as the measurement resolution of a velocimeter, is fairly poor, even in this application. However, this was a very early stage experiment and the first level proof of concept.

The x-axis of Figure 3.5 is very telling in terms of the problems this sensing method has in terms of time resolution. Profiles such as this one, where the measured frequency closely follows the induced (actual) frequency of the light could only be collected for piezo-tuning frequencies of 50 Hz or slower, while tuning over a small range of piezo-stack displacements. At higher tuning frequencies, the WGM signals would begin to deteriorate and then would be destroyed entirely. It is hypothesized that this was the product of three different effects: At intermediate frequencies, close to, but above 50 Hz, the WGM resonances would become unstable, that is they would not settle to a single location in the spectrum, which is likely the effect of the deformation of the microresonator lagging behind the forcing of the piezo-stack due to viscoelastic effects. At frequencies much higher than 50 Hz, we were unable to identify WGM resonances. This may have been due to the fact that the piezo-stack lost contact with the resonator during its tuning cycle and, instead of continuously and smoothly forcing the resonator, was forcing the resonator via periodic impulses. Alternatively, the mechanical forcing may have destabilized the coupling connection with the optical fiber, which would cause different azimuthal and equatorial modes to be excited at different times, preventing the identification of resonance shifts. As a result of these effects, measurements could be taken maximally once every 0.02 seconds, which was deemed too low to be practical since in the final design many hundreds of scans are expected to be needed, in order to ensemble average the discrete Mie scattered signal, to make a measurement. While the piezo-modulation of resonances worked, it immediately became clear that there were several problems, including the low frequency response of the resonator to deformation by the piezo-stack and the subsequent effect this would have on the time resolution of a final sensing system. Rather than pursue a potentially untenable system design, we re-adjusted to take advantage of the wavelength tuning features of our laser.

3.2. Laser-Modulated Resonance Excitation with Rotating Disk Target

This is the next level of proof of concept, where actual velocity measurements are made on the edge of a rotating disk. Given the low time-resolution of signals that a piezo-modulation based approach entailed (even in the best of circumstances), here we decided to opt for a laser-modulated approach, since this would increase the time-resolution of the sensor significantly, as the integration time of this approach is only limited by photon flux through the detection lenses and can therefore always be improved by more and more powerful lasers.

3.2.1. Experiment

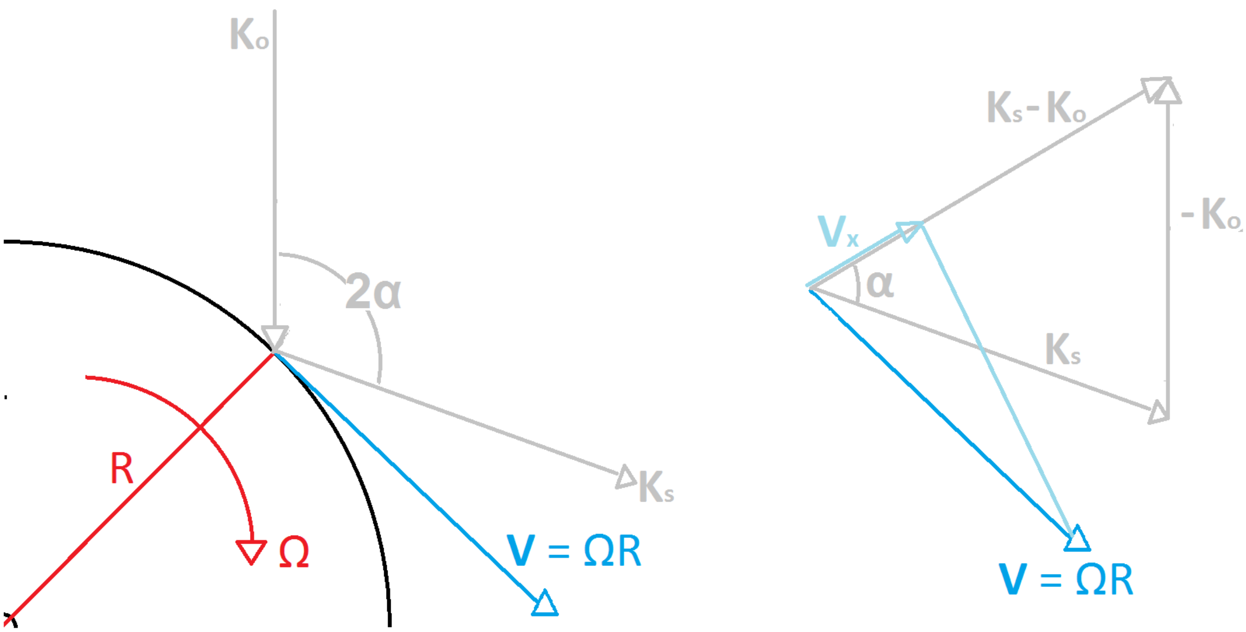

Figure 3.6. Vector Diagram of Doppler Shift Measurement from a Rotating Disk

In this experiment, we demonstrate the detection of Doppler shifts of light scattered from a (solid) moving target as a proof-of-concept for this sensing system. In order to take advantage of the high WGM Q-factors of our microresonators and detect small Doppler shifts, we used a narrow linewidth laser aimed at a target location and in the desired measurement direction. The scattered light from the target location is collected and fed (via side coupling) into the microresonator. As the laser frequency is tuned over a narrow range, the optical modes (WGM) of the resonator are excited by the surface-scattered light. The fiber serves as an input-output device, and is connected to a free-space-to-fiber-coupler on one end and a photodiode on the other. The WGM are observed as dips in the transmission spectrum through the fiber. The shifts of these WGM relative to a reference indicate the Doppler shift of the collected light which can be related to the relative speed of the target. The vector diagram shown in Figure 2.10 of Section 2.4 is reproduced in Figure 3.6 with a rotating disk as the target. That is, the generalized moving target is replaced with the more specific situation of the rotating disk target.

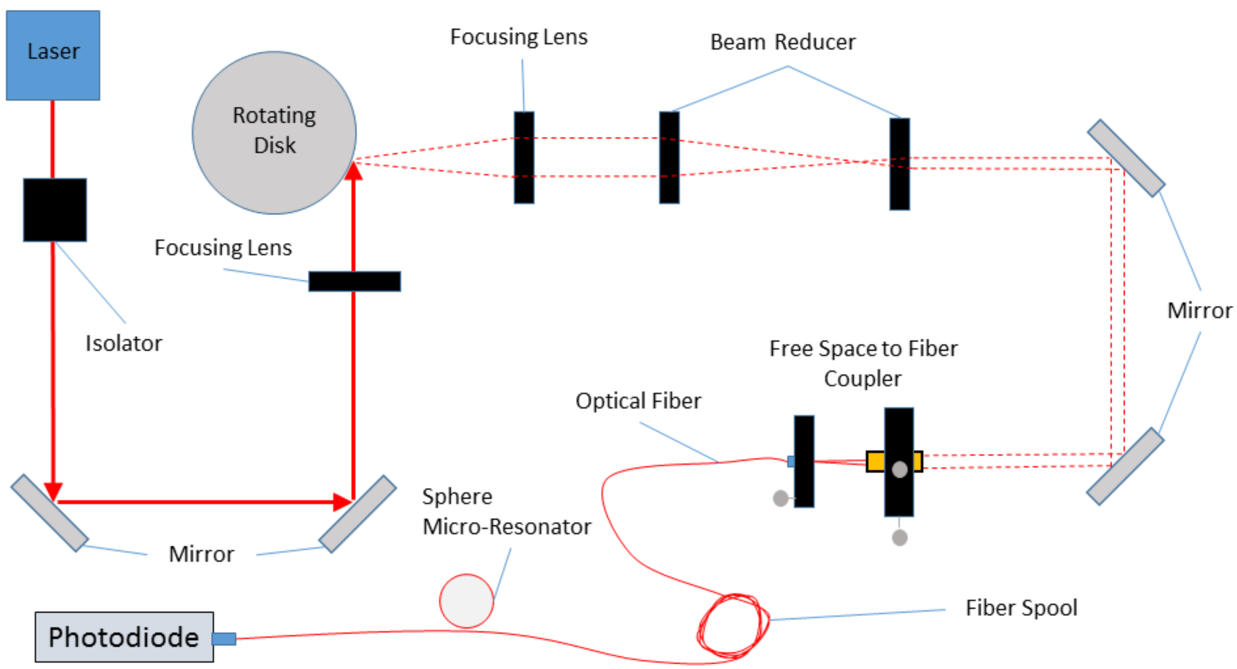

Figure 3.7. Schematic of Laser–Modulated Experimental Setup

This experimental setup (Figure 3.7) is designed to show that the WGM microresonator–based velocity sensor is capable of measuring Doppler shift from scattered laser light. We use the edge of a spinning hard drive disk as the moving target. This time a narrow-line visible laser is used. The laser beam from a 9mW, 639nm Littman-Metcalf cavity diode laser (New Focus Vortex TLB 6800), with a line width of 200 kHz, is focused on the edge of the rotating disk. Disk angular velocities ranged between 45–240 rotations per second (corresponding to edge tangential velocities of 15–75 m/s). Angular velocities less than 45 rotations per second were difficult to control, as the angular velocity of the HDD disk did not stabilize. Doppler–shifted scattered light is collected with a certain cone angle, collimated, and subsequently reduced in diameter to couple it into a single mode (SM) optical fiber as shown in Figure 3.7. The mode field diameter of the SM fiber is between $3.6 - 5.3\mu$m depending on the precise wavelength of the light in the fiber. [35]

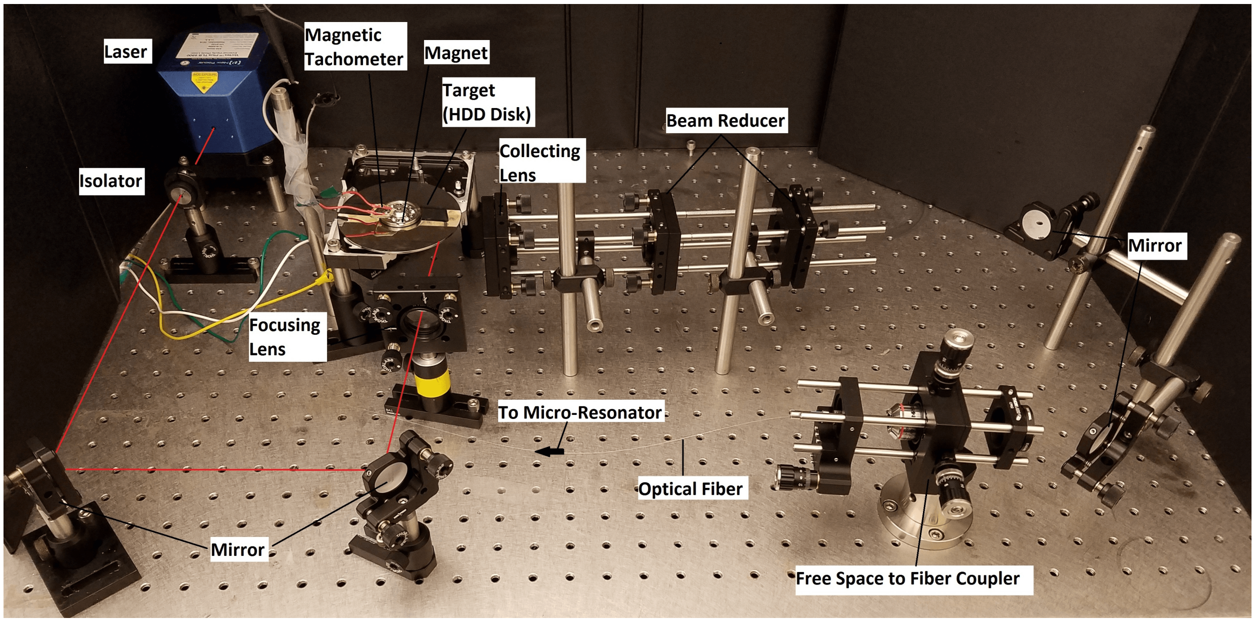

Figure 3.8. Laser–Modulated Experimental Setup

After fiber coupling, light is directed through a tapered section of fiber (as in Fig. 2.4), where it is coupled into a spherical silica microresonator, with diameter of $\sim 500\mu$m, acting as an ultra-high resolution interferometer. The transmitted light is detected by a photodetector (ThorLabs # PD36A) and its output is discretized by a 12 bit analog-to-digital converter with the same system used in Section 3.1.1. The data is stored and analyzed, and the system is controlled by, a data acquisition system running on a desktop computer. A photograph of the optical setup is shown in Figure 3.8 with labels and an artificial laser beam added for clarity. A magnetic tachometer is used, in conjunction with a digital oscilloscope, to accurately determine the rotational frequency of the disk.

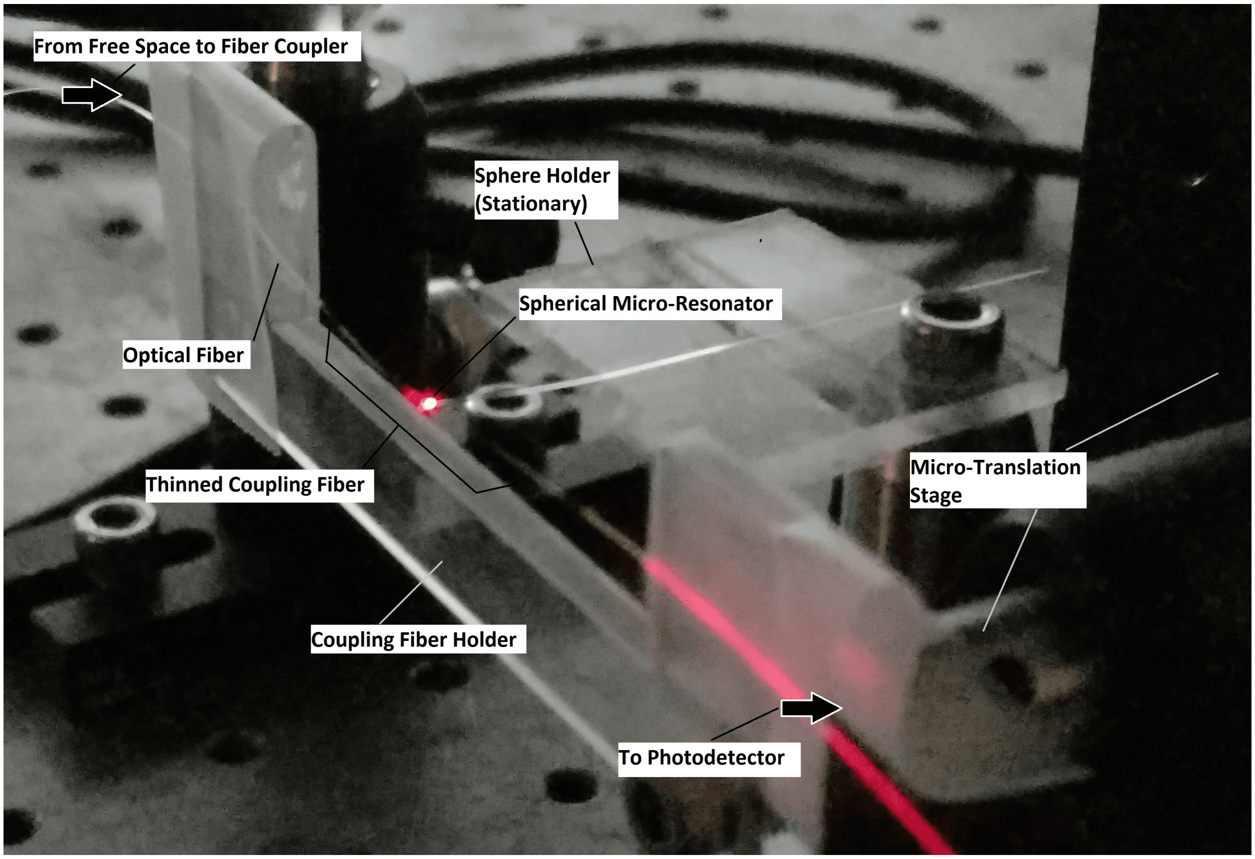

Figure 3.9. Laser-Modulated Experiment Fiber-Microresonator Coupling

Figure 3.9 is a photograph of the microsphere resonator and the coupling fiber. Noteworthy are the large amounts of light lost to scattering at the sphere and the loss of light from coupling between the sphere and the single mode fiber, seen downstream of the sphere and towards to the photodetector. Any light seen by the camera taking the picture in Figure 3.9, is not seen by the photodetector and is therefore lost. The laser's nominal output power is 9 mW and approximately 1.6 mW of light scattered from the disk edge is captured by the collecting optics. From this, about 13.5 μW of the light is coupled into the SM optical fiber (before tapering). The amount of light detected by the photodetector (after fiber tapering) during the measurements is 0.05 μW, representing a light loss of $\sim$ 99.63% between collection aperture (the total usable scattered photon flux) and photodetector (usable measurement photon flux). Clearly, optical coupling efficiency at the various stages is a challenge in the present system.

3.2.2. Results

Using the setup described above, a set of experiments were performed with different disk rotational speeds. A summary of these results is presented in Figures 3.10 and 3.11. Generally, the WGM are seen as a series of dips through the transmission spectra (photodiode output) as we tune the narrow-line interrogation laser, in this case one dip is shown to demonstrate efficacy of the system. The WGM shifts between the spectra, relative to the minimum speed spectrum, are proportional to the Doppler shift of the scattered light from the target.

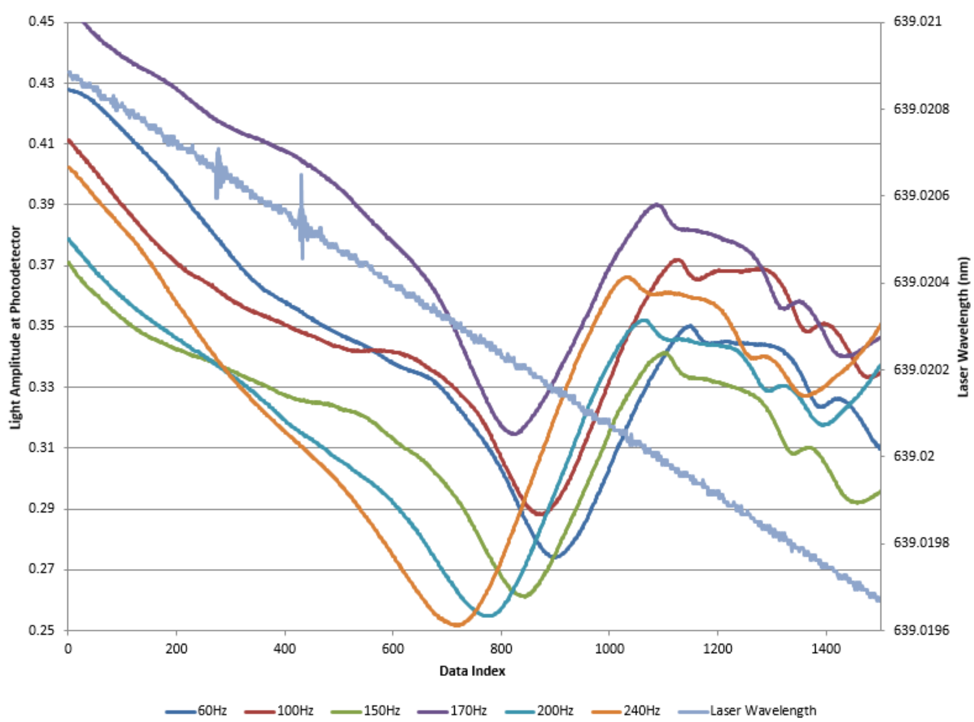

Figure 3.10. Transmission Spectrum around Selected WGM Dip

The laser was scanned at a rate of 700 Hz (using a ramp/triangle waveform). Across each scan of the laser, 6000 digitized data points were recorded to form transmission spectra (in a phase-locked way, such that the data index of each point corresponds to the same emitted laser wavelength). Figure 3.10 shows a subrange in the transmission spectra that captures a single WGM at various disk frequencies, along with the corresponding laser wavelength (negative ramp signal). As the disk's rotational frequency increases, the WGM resonance moves to the left (longer wavelengths) due to Doppler shift. The curve for each disk frequency shown in the figure is an ensemble average of approximately 600 successive scans of the laser. Due to photon shot noise (weak light power incident on the photodetector) and the wobbling of the disk (which results in variable signal strength and signal dropout through each revolution of the disk), it was not possible to discern WGM of the microsphere through the transmission spectrum from each individual scan of the laser alone. Thus, ensemble averaged transmission spectra are used to determine the WGM and the Doppler shifts. The total duration for each measurement is on the order of a second. Note that the light amplitude at the photodetector is in arbitrary units, due to the variance of light levels for subsequent scans caused by the disk's beam steering.

Figure 3.11 shows WGM shifts (corresponding to the Doppler shifts) of the data of Figure 3.10. This figure presents three different approaches of determining dip location, along with the least squares regressions for each resonance shift detection method. In the manual dip detection (MDD) method, WGM shifts are determined manually (or visually) by selecting the location of the minimum value of each dip. While this method seems fairly arbitrary at first, the human brain is much less likely to be confused by a stray data point (caused by noise in the data) than a computer. The automatic dip detection (ADD) method uses software to choose the absolute minimum value in each data vector (ensemble averaged scan), which is much faster than MDD, but may be challenged by noisy data. In the last method, cross–correlation (CC) is performed between each data vector and a reference data vector. There is good agreement between MDD and ADD results. The CC results show slightly lower Doppler shifts and have a larger scatter, which perhaps indicates that further signal

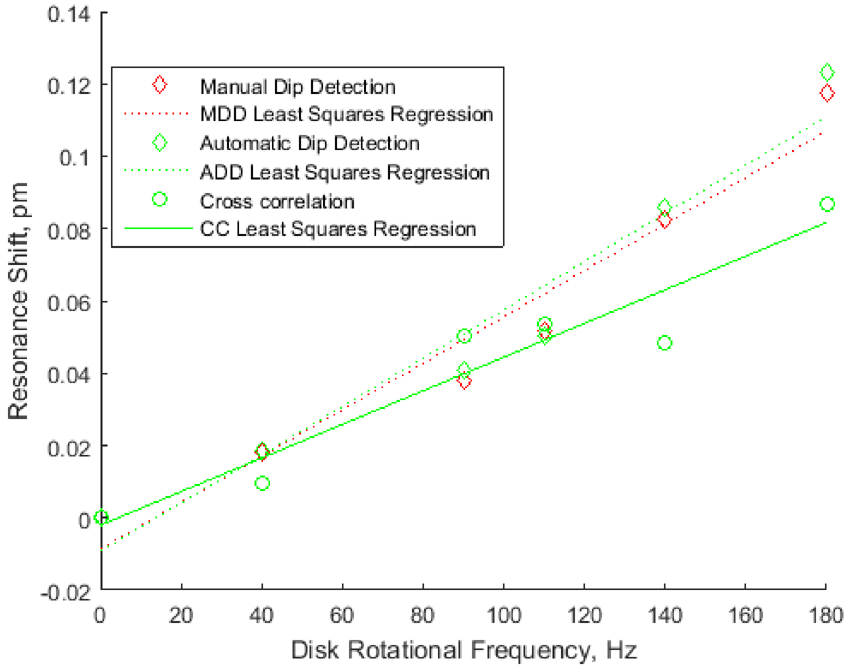

Figure 3.11. WGM Shift vs. Disk Rotational Frequency for Data of Figure 3.10

processing and/or an increased number of resonance features are required to allow a more robust cross–correlation approach. The cross-correlation approach generally is preferable to the ADD method, given that it is less susceptible to noisy data, and can be computationally less demanding than other signal processing methods.

Spline fitting of the resonance dips was also attempted and produced accurate results for individual resonance centers. However, programmatic limitations of automatic spline fitting to order five or less restrict their use to single resonances, whereas the CC method can analyze an entire scan (and tends to produce more accurate results using signals containing multiple resonances). Although spline fitting of resonances is a possible avenue of signal processing for this experiment (and will be explored further in future experiments), at present, cross–correlation is the preferred method for shift detection given its ability to analyze whole scans without human interaction and with relatively low computational effort.

Also, we note that due to the high optical quality factors possessed by the microresonators, very small changes in the target velocity can be determined. With a quality-factor of $\sim 6 \times 10^6$, which is imminently achievable in a laboratory setting, and using the cross-correlation algorithms developed at the MicroSensor Lab at SMU, current estimates for wavelength resolution are on the order of $\sim 10fm$. This current preliminary result indicates that, for a back-scatter LIDAR system using a side-coupled WGM resonator, a velocity resolution of $\sim 2.4m/s$ is possible. This value is based on a full, or nearly full, backscatter configuration, where $\alpha \to 0°$.

Chapter 4

FREE-SPACE COUPLED RESONATOR EXPERIMENTS

In previous sensor development efforts, such as the electric and magnetic field sensors [14] and the seismometer [10], designed at the Micro-Sensor Lab at Southern Methodist University, the optical sensors have always utilized direct fiber coupling, as in Figures 2.4 and 3.9, which resulted in a coupling signal that was stable in time with respect to the stability of the laser diode. However, in the experiment discussed in Section 3.2, intermittent signal loss (drop-out) was observed due to difficulty in reliably coupling scattered light into a single mode fiber with a very small numerical aperture, as will be shown in Figures 5.2 and 5.3 in the next chapter. As previously discussed, this signal loss was due to beam steering, occurring due to the imperfect motion of the rotating disk and the precise nature of coupling from free space to a single mode fiber.

4.1. Experiment

In order to make the sensor design more robust, additional experiments were carried out in which free-space light is coupled into the resonator, as shown in Figure 4.1 and 4.2. WGMs were observed through scattering from the sphere instead of the transmission through the coupling fiber. This corresponds to the scattering spectrum in Figure 2.5, rather than the transmission spectrum which was measured previously.

Since we have previously demonstrated the ability to measure the velocity of a moving target, our new setup omits the moving target. By modulating the central wavelength of the laser (in addition to scanning the laser in order to tune the resonator), effectively simulating the moving target, we can easily omit the target while still demonstrating the efficacy of a free-space coupled system. The free-space system, given its reduced sensitivity to beam steering (which will undoubtedly occur in a final design that is intended to measure

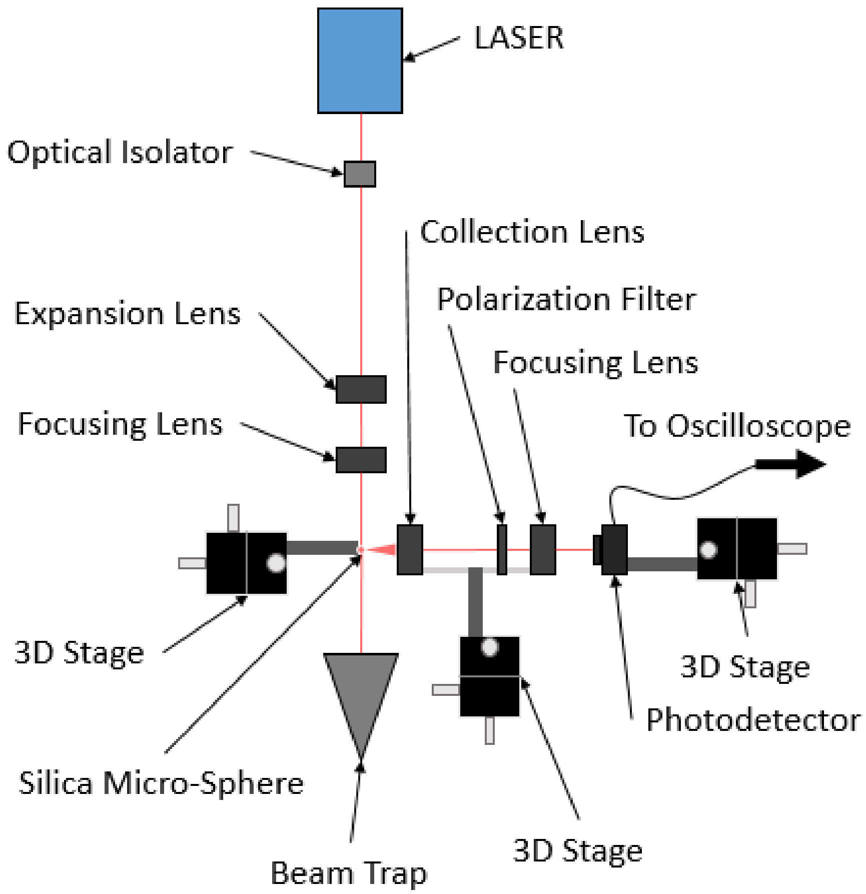

Figure 4.1. Schematic of Free Space Coupling Experiment

the relative velocity between a spacecraft and atmospheric particles), shows that there are various options which do not depend on coupling into a single mode optical fiber, greatly increasing the potential robustness of any final measurement system.

In this preliminary test, we focus the same visible wavelength laser light on to the side of the sphere resonator and capture the light scattered from the sphere, which is directed onto a photo–detector, as shown in Figure 4.1. A portion of the scattered light should be from that coupled into the sphere tangentially. An expansion lens and a focusing lens are used to minimize beam waist at the microresonator to increase the amount of light coupled into the resonator tangentially. Therefore, as the laser frequency is scanned the WGMs of the

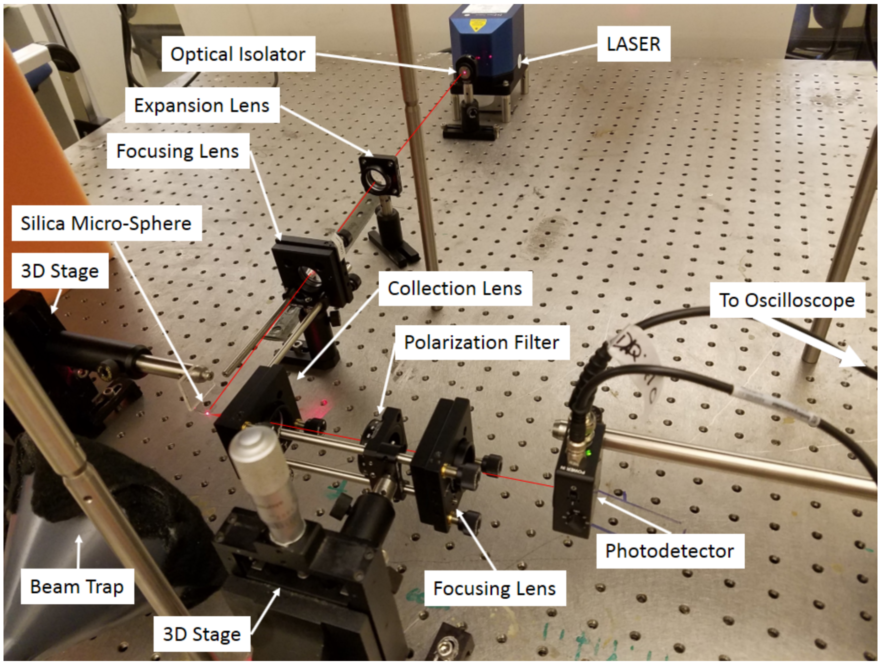

Figure 4.2. Free Space Coupling Experimental Setup

sphere should be observed in the scattered light. An added complication of this method of resonator coupling is the amount of background signal being received by the photodetector from Mie scattering off the resonator itself. While ambient light is fairly easy to exclude by isolating the resonator and photodetector from the surroundings, imperfect coupling of the light means that there is a large amount of light scattered containing no WGM information. Fortunately, some of the background light signal can be eliminated using a polarization filter and by controlling the inlet and exit pupil diameters (virtual aperture) to minimize the field of view of the photodetector to contain only the resonator and not reflections of the scattered light.

4.2. Results

Figure 4.3 demonstrates that using a silica microsphere excited via free-space laser light as described above, we can detect a shift in the wavelength of the light irradiating the

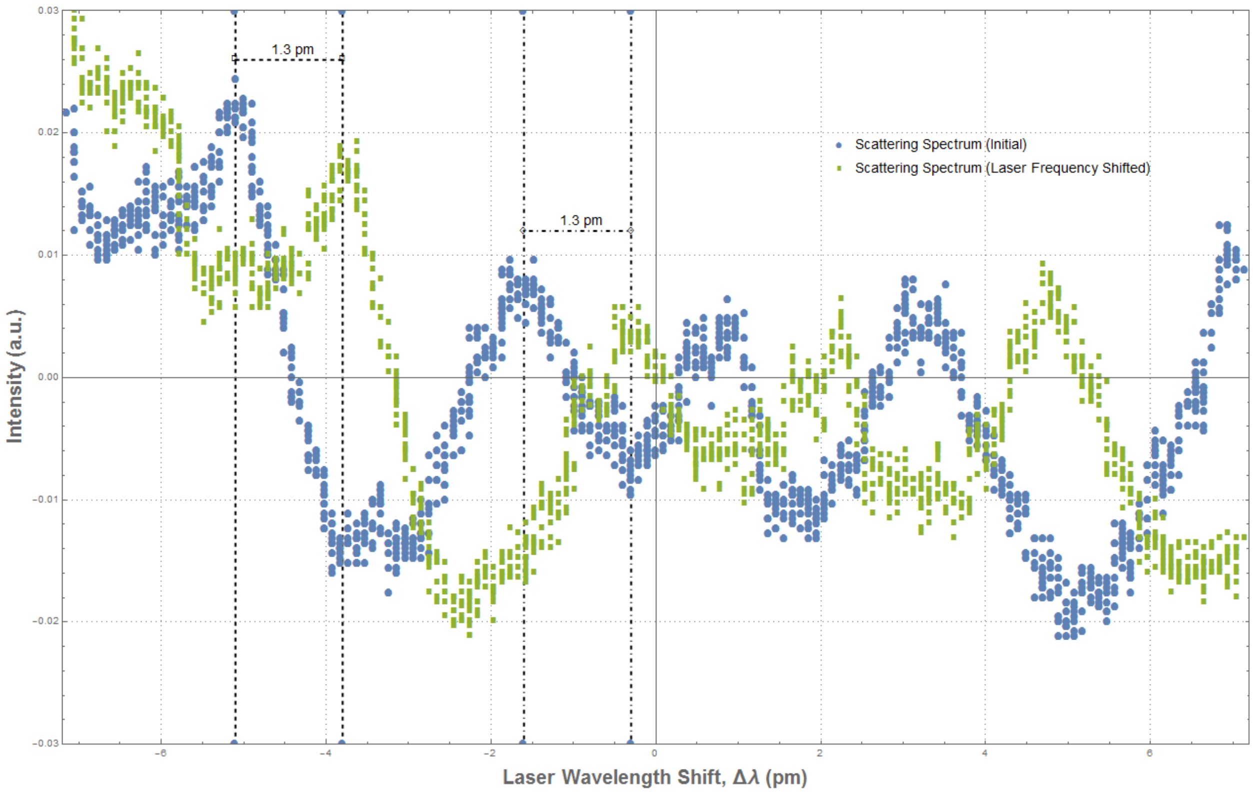

Figure 4.3. Free Space Coupling Results

sphere by observing the shift in the WGM in scattered light, as explained in Section 2.4. The figure shows the resonance spectrum produced by a triangle waveform (described by $\lambda_{Initial}(t) = \lambda_{Center} + m \times t$, for any given linear section of a scan) about the central wavelength of our laser (in blue). Additionally, in Figure 4.3 we have imposed a shift, $\Delta\lambda_{Doppler} = 1.3pm$, on the center wavelength of the interrogation laser (simulating a Doppler shift), such that $\lambda_{Shifted}(t) = (\lambda_{Center} + \Delta\lambda_{Doppler}) + m \times t$ which is responsible for the laser frequency shifted scattering spectrum (green). Measurement of the wavelength delay between features (corresponding to resonance modes of the microsphere) in the initial and shifted scattering spectra allows us to determine the corresponding wavelength shift of the incoming light due to $\Delta\lambda_{Doppler}$. Given the fact that resonance wavelengths are nearly constant in time for a given resonator (assuming it is not undergoing large temperature or morphological changes), we know that the apparent shift in resonance wavelength $\Delta\lambda_{measured} = \lambda_{Shifted}(t) - \lambda_{Initial}(t) = \Delta\lambda_{Doppler}$. We can see from Figure 4.3 that there is very good agreement between the imposed *Doppler*-shift and the calculated shift from the scattering spectra, as the imposed $\Delta\lambda_{Doppler} = 1.3pm$ exactly corresponds to the measured shift in the spectrum, $\Delta\lambda_{Measured} = 1.3pm$. Therefore, in principle, Doppler shift measurements can be made using free space coupling of scattered light into the resonator. More study is required in this area to ascertain whether the benefits of using a free space system, increased light level and decreased vibration sensitivity, outweigh the disadvantages of increasing the background noise level produced by the resonator. These results indicate a critical design choice between a system with larger available light levels, of which a large portion is an unusable, static DC component caused by Mie scattering from the resonator itself (the free-space system), versus a system with a higher intrinsic signal-to-noise ratio, but significantly lower light levels (the fiber-coupled system). The combination of free space coupling with the signal processing methods discussed in Chapter 5 is expected to yield better results than a fiber coupled system, despite low coupling efficiency.

Chapter 5

SIGNAL PROCESSING APPROACHES

5.1. Cross–Correlation

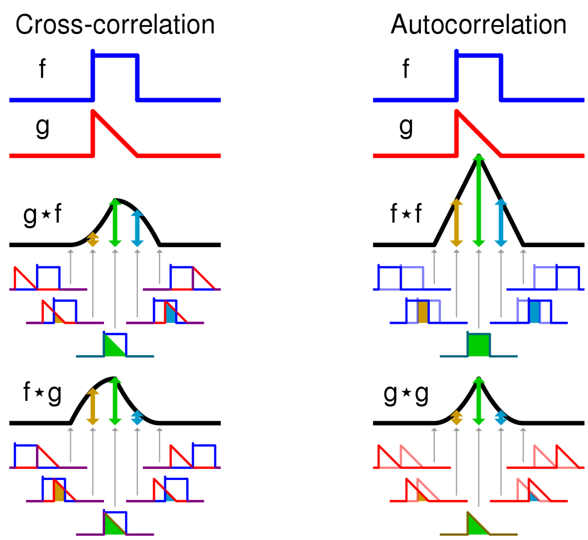

Figure 5.1. Comparison of Cross-Correlation and Auto-Correlation [38]

Cross-correlation is a signal processing technique often applied to statistical data sets and in the field of image processing. A pictoral explanation is shown in Figure 5.1. In essence, the cross-correlation of two functions or data sets, f and g, gives another function or data set $h \equiv g \star f$ that shows how overlapped the two data sets are when they are shifted with respect to one another. In Figure 5.1 this is shown as the overlap of the square wave, f, and the ramp signal, g. When the two functions are shifted such that none of their areas overlap, the cross-correlation is zero. However, as the signals are shifted such that their areas overlap, the cross-correlation strength grows to its maximum when they are maximally overlapped, as in the green vector in Figure 5.1. Auto-correlation is simply a specific subset of cross-correlation, where the cross-correlation algorithm is applied to the same function rather than two different ones. Two examples can be seen on the right hand side of Figure 5.1. Various two-dimensional versions of the cross-correlation algorithm exist, however, of interest in this thesis is the one-dimensional algorithm given in Equation 5.1.

$$\hat{h}_d = \sum_{n=-\infty}^{\infty} \hat{\chi}_n \hat{\xi}_{n+d} \tag{5.1}$$

This algorithm takes as an argument two vectors, $\hat{\boldsymbol{\chi}}$ and $\hat{\boldsymbol{\xi}}$, which in general could be any one dimensional vectors, functions, or data sets, but in this case represent two WGM spectra. The subscripts n and d represent the n-th and d-th elements of the vectors. The sum in Equation 5.1 is computed over a range of delays, d, generating the cross-correlation waveform, $\hat{\boldsymbol{h}}$, a one dimensional vector of length $x + z$, where x and z are the lengths of $\hat{\boldsymbol{\chi}}$ and $\hat{\boldsymbol{\xi}}$, respectively.

The elements of $\hat{\boldsymbol{h}}$, the cross-correlation waveform, then represent the degree of correlation between the vector $\hat{\boldsymbol{\chi}}$ and the shifted vector $\hat{\boldsymbol{\xi}}'$, where the elements of $\hat{\boldsymbol{\xi}}'$ are equal to the elements of $\hat{\boldsymbol{\xi}}$ shifted to the right (or left) by delay d. Therefore, the absolute maximum of $\hat{\boldsymbol{h}}$, corresponds to a given delay d_{max}, which is the value of the delay with which the two spectra are most strongly correlated. When auto-correlation is performed, that is $\hat{\boldsymbol{\chi}} = \hat{\boldsymbol{\xi}}$, the absolute maximum corresponds to the null-shift, i.e. $d_{null} = 0$. [1] If the cross-correlation of two WGM spectra taken at different times is computed, the difference $\Delta S = d_{max} - d_{null}$ gives the amount of shift, ΔS, corresponding to the change in tuning required to counteract the Doppler shift which has occurred in the time interval between the two scans. Then, with the knowledge of the tuning parameters and the response of the resonator, the Doppler frequency shift can easily be determined.

5.2. Variance Filtering

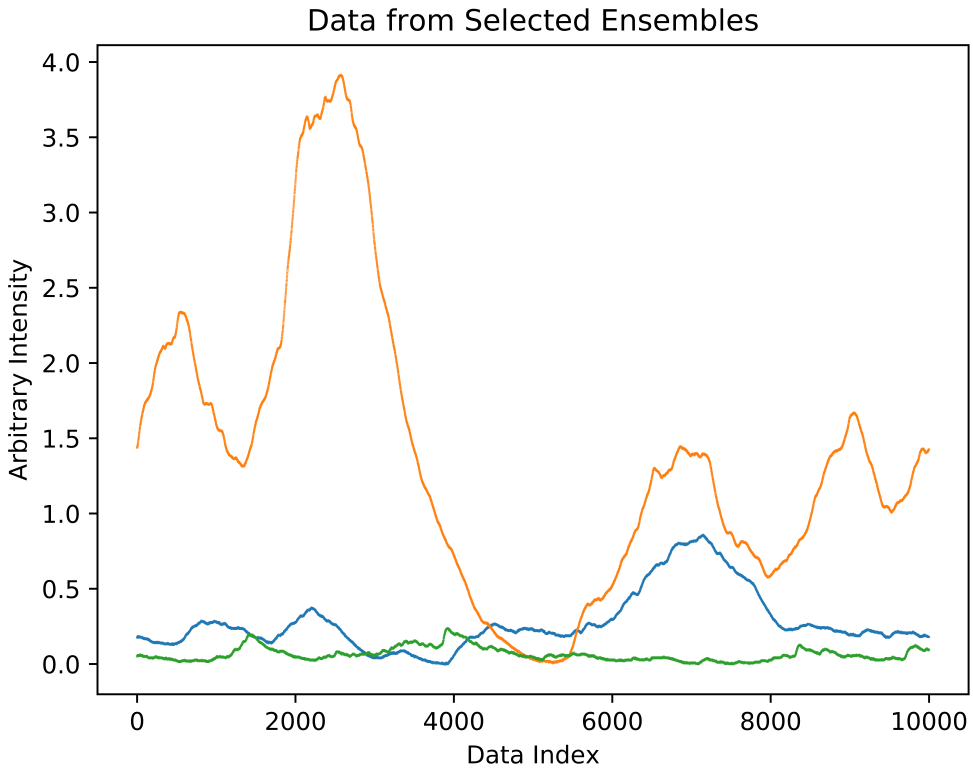

Figure 5.2. Signal Processing Motivation: Selected Scans with High Variance (Orange), Marginal Variance (Blue), and Low Variance (Green)

As discussed previously, signal degradation and dropout caused by undesired beam steering and coupling issues were experienced. It is anticipated that the conditions which led to this signal degradation in the laboratory will also be present in the final application. The problem was especially acute in the fiber-coupled experiment due to the high precision required in free-space to single-mode fiber coupling of scattered light from the disk surface. Fortunately, the fiber-coupled experiment allows for a realistic test of this measurement approach. In the Mie scattering regime the scattered signal is discrete. Also, due to atmospheric turbulence, beam steering will likely cause signal dropout. Clearly, however, a more robust signal processing method, in conjunction with the proposed physical design improvement of free-space coupling, is required in order to increase the reliability of the measurement system. Figure 5.2 shows three individual raw scans from the same data set, taken no more than a few milliseconds apart (each representing a single laser scan). In orange we see what a typical WGM spectrum looks like, a fairly complex signal with many distinct peaks and valleys. In blue is a scan that potentially has some interesting information, particularly between indices 6000 and 8000, but otherwise appears to be mostly background noise. Green shows a spectrum that is almost completely background noise. These are three representative scans of the over 600 scans collected for a given disk speed. Most likely, in the case of the green scan, no scattered light from the disk was coupled into the optical fiber across the full scan of the laser. Some scans contain excellent information, some contain intermittent information, and some contain little or no information.

For the results shown in the previous sections (Figure 3.10), the only data processing done is phase locked averaging of the 600 individual scans to obtain an ensemble of the transmission spectrum at a given disk speed. We then compare this ensemble (either manually or via cross–correlation) to a previous measurement to determine the shift in wavelength of the resonances, and finally, via calibration of the laser, we relate this shift to some change in the quantity we want to measure. Clearly, with an intermittent signal such as this one, this approach may not be sufficient for reliable measurements. Therefore a more robust method (which is not computationally taxing due to constraints on the final measurement system) is needed to determine whether a scan has enough interesting information (a high enough signal-to-noise ratio) to warrant analysis.

While several different signal processing methods were explored, most were deemed likely to be too computationally taxing to be useful in the final application. However, one of the key observations that was made by looking at the raw data, as in Figure 5.2, was that even signals with a fairly low mean signal level contained usable information (as in the second half of blue scan in 5.2). By examining a large subset of the scans, it was found that the mean square variance of a scan, given by

$$\sigma^2 = \frac{1}{N}\sum_{i=1}^{N}(x_i - \mu)^2 \tag{5.2}$$

is a good predictor of whether the scan contains WGM information or not. The mean square variance meets our criteria for being computationally lightweight as the computational complexity of Equation 5.2 is $\mathcal{O}(n)$, meaning that the computational cycles required to find the variance of a set grows linearly with the number of elements in the set, n. In comparison, the computational complexity of determining the cross-correlation of Equation 5.1 is $\mathcal{O}(n^2)$. This means that for any set with significantly large n, the computational complexity of determining the variance is negligible compared to the complexity of the cross-correlation itself.

Observing Figure 5.2, the scans with no or small portion of signal dropout (orange trace), have strong features in the transmission spectrum, hence have large (mean square) variance. Analysis of the variances of all 600 scans in one data set (all taken at the same disk speed) is shown in Figure 5.3 in the form of a histogram. A large number of scans show very low variance, so much so that the first bin in Figure 5.3 has over three times more scans than any other bin. We hypothesized that by choosing only high variance scans for use in our ensemble averaging, our signal-to-noise ratio (due to signal dropout) would improve, resulting in signals that are better suited for cross–correlation. Therefore, the variance of any given scan can be used as a filter by introducing a cut-off variance below which a scan is discarded. This filter, combined with phase-locked ensemble averaging used previously, is intended to reduce the stochastic error of each scan by taking a large number of scans and ensemble-averaging them, thereby mitigating signal dropout effects, without degrading essential spectral information. Of course one potential drawback of this approach is that if, at a given cutoff variance, the usable number of scans becomes too small, cross-correlation would not be accurate.

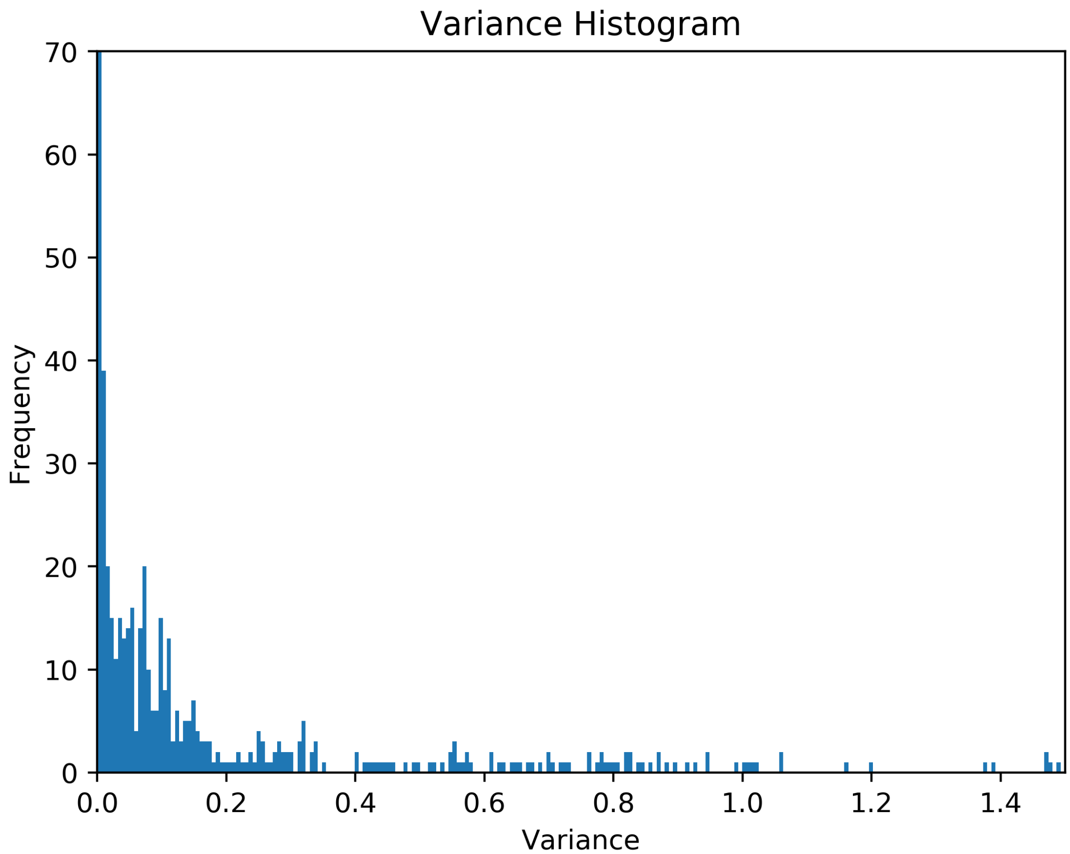

Figure 5.3. Signal Processing Motivation: Histogram

5.3. Results

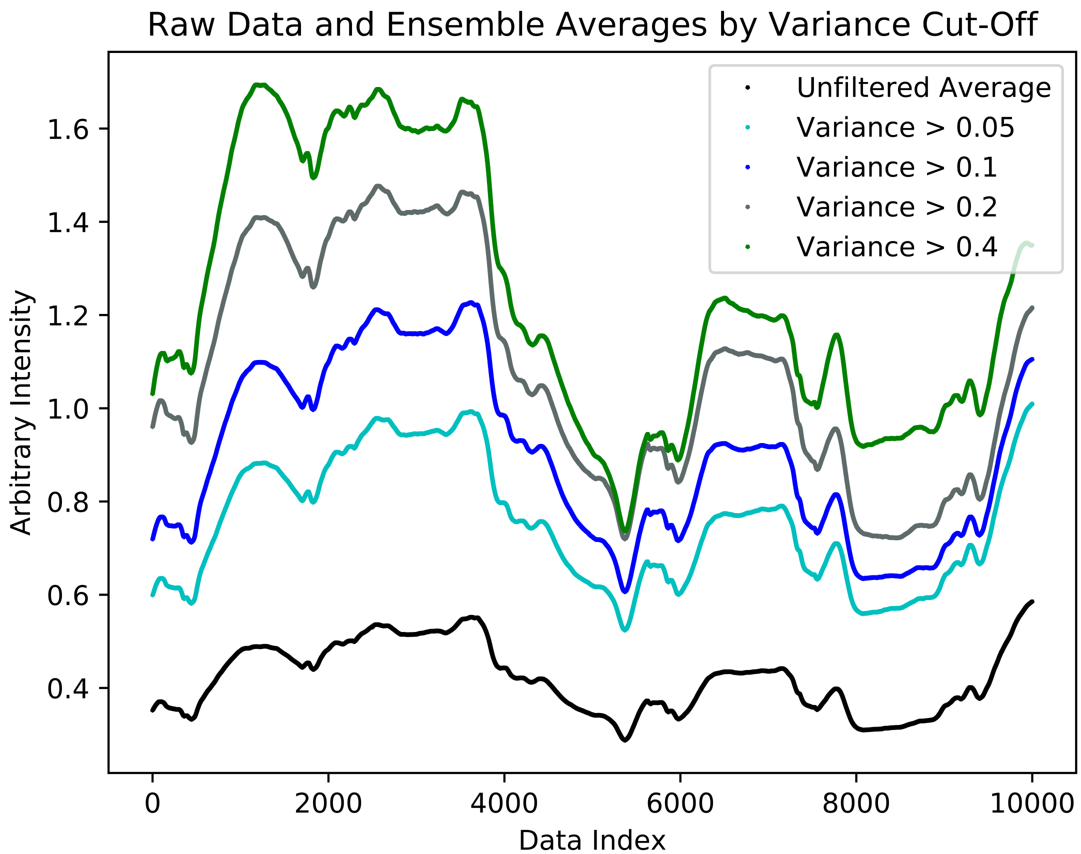

Figure 5.4. Variance Filtering Signal-to-Noise Ratio Improvement

Figure 5.4 shows the unfiltered ensemble average in black, and various filtered ensemble averages in different colors. The figure offers interesting observations: Firstly, features are increasingly crisp and more distinct as the cut-off variance is increased. This indicates that the variance filtering approach is successful, at least to visual inspection, in increasing the signal-to-noise ratio of the ensemble averaged scans. This is an anticipated result, as removing signals with low relief, i.e. signals that are more flat, prior to averaging increases the relief of the averaged signal.

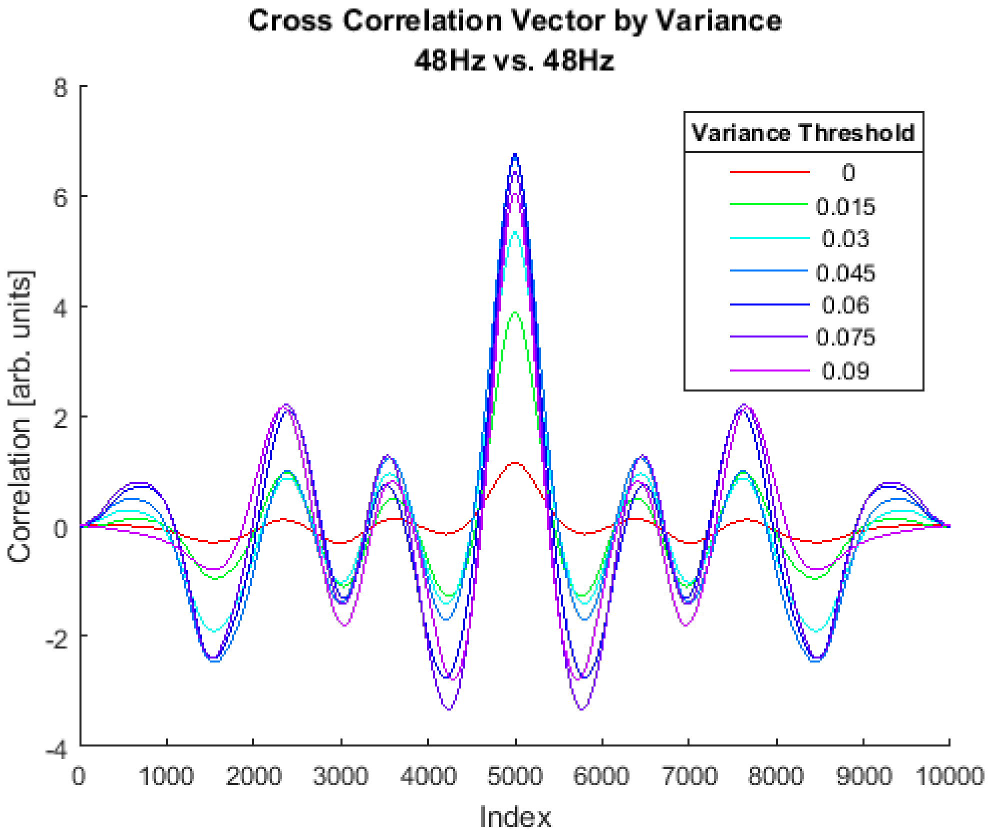

Figure 5.5. Auto-Correlation Results for Various Variance Filtering Thresholds

Figure 5.5 shows several auto-correlations of the same date (ensemble averaged scans) with different variance filters applied before auto-correlation. Several observations can be made from Figure 5.5. Most importantly, the fact that our variance filtering results show a dramatic increase in the correlation strength means that the variance filtering method does improve the signal-to-noise level of the data set when it comes to calculating the auto-correlation. This is an excellent result given the fact that the ability of auto- and cross-correlation to detect shifts between two spectra is directly linked to the sharpness of the global maximum in a correlation vector, like the one plotted here. Another interesting result that can be gleaned from this figure is the fact that the highest variance filtering threshold in this figure does not yield the highest correlation. While this may seem to argue against the use of this signal processing method, it actually acts as an important sanity check for the following reasons: Firstly, as the cut-off threshold of the variance filter is increased, naturally, the number of ensembles being averaged is decreased. As mentioned earlier, this decrease in the number of ensembles, given the high degree of variability between ensembles, means that as the number of ensembles being averaged decreases, the ability of averaging to compensate for the stochastic error in the signal decreases. Therefore, we can easily see that there are two effects which drive the selection of the variance filtering threshold. Weak correlation peaks at low filter thresholds require increasing variance thresholds to increase correlation strength, while inability to form a representative average due to the stochastic nature of the signal requires a high number of ensembles in the average, indicating the need for a lower filter threshold or a higher integration time. Optimal cut-off thresholds, therefore, are expected to be at some intermediate value, which we can see in the results of Figure 5.5 and will also be evident in the results of Figure 5.8 later on.

Figure 5.6 shows the results of cross-correlation of two different data sets (at disk angular speeds of 120 rotations per second and 48 rotations per second) and confirms many of the conclusions found from Figure 5.5. Of note, again, is the increasing strength of the signal correlation, as well as the fact that the maximum variance does not correspond to the maximum correlation. A feature that was not previously seen that is visible here is the fact that for the plain ensemble averaged signal, the peak at index 4700 (the anticipated global maximum) is actually slightly smaller than the peak at index 3600. This phenomenon is one of the shortcomings of the cross-correlation approach. For periodic signals with weak correlation, it is possible for the algorithm to accidentally select the incorrect cross-correlation peak, in a phenomenon that can be thought of as analogous to a mode hop of the algorithm. However, with stronger correlation of the two signals (as shown in Figure 5.6) and the signal processing approaches designed for optimizing cross-correlation previously developed in our lab (not used here in order to demonstrate this effect), this phenomenon can be overcome. More discussion on this subject can be found in theses of Dr. Ali and Mr. LaPenna. [1,20]

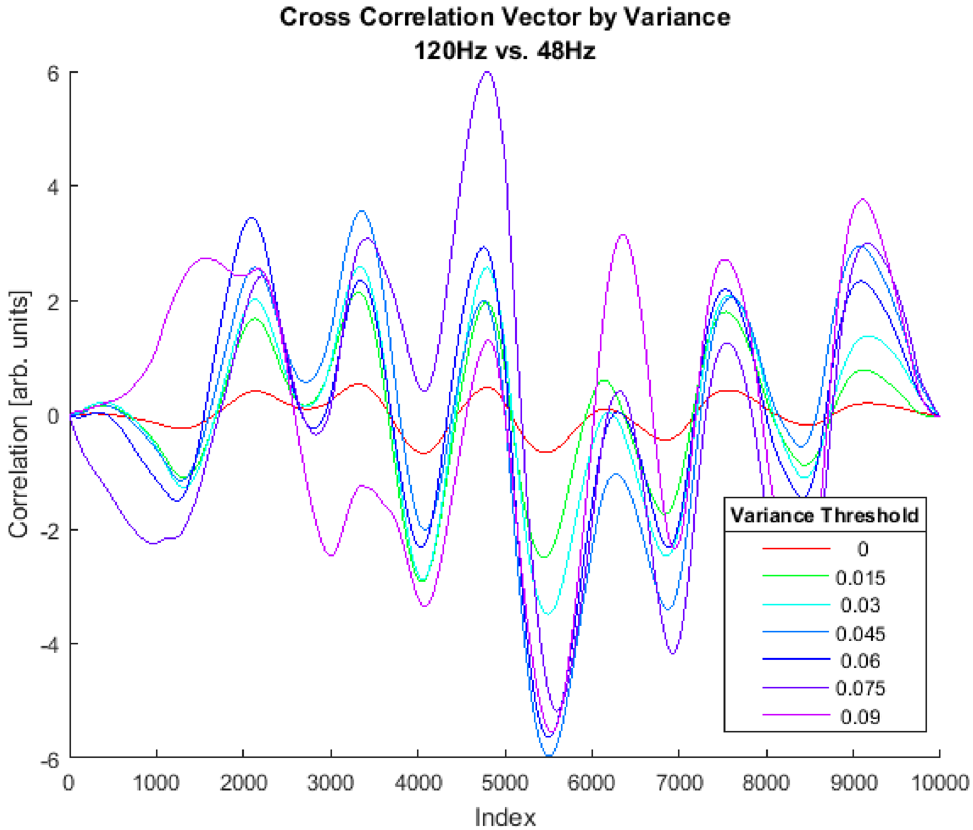

Figure 5.6. Cross-Correlation Results for Various Variance Filtering Thresholds

The efficacy of this signal processing approach is demonstrated in Figures 5.7 and 5.8. Figure 5.7, shows the results of the cross-correlation algorithm, with various different cut-off thresholds as well as the results of manually attempting to determine the disk velocity from an unfiltered WGM spectrum. Also shown are the actual or calculated shift given the disk rotational frequency, calculated from Equation 2.5 and upper and lower bounds for the actual value. The upper and lower bounds are calculated as worst case bounds from the geometry of the setup, specifically the incident and scattered light vectors and the local direction vector of the target. The bounds represent $+15°$ and $-15°$ in plane variances of the angles α and θ, which is defined as the angle between the local target velocity vector and the measurable component of the target velocity. While these bounds may seem generous, it is important

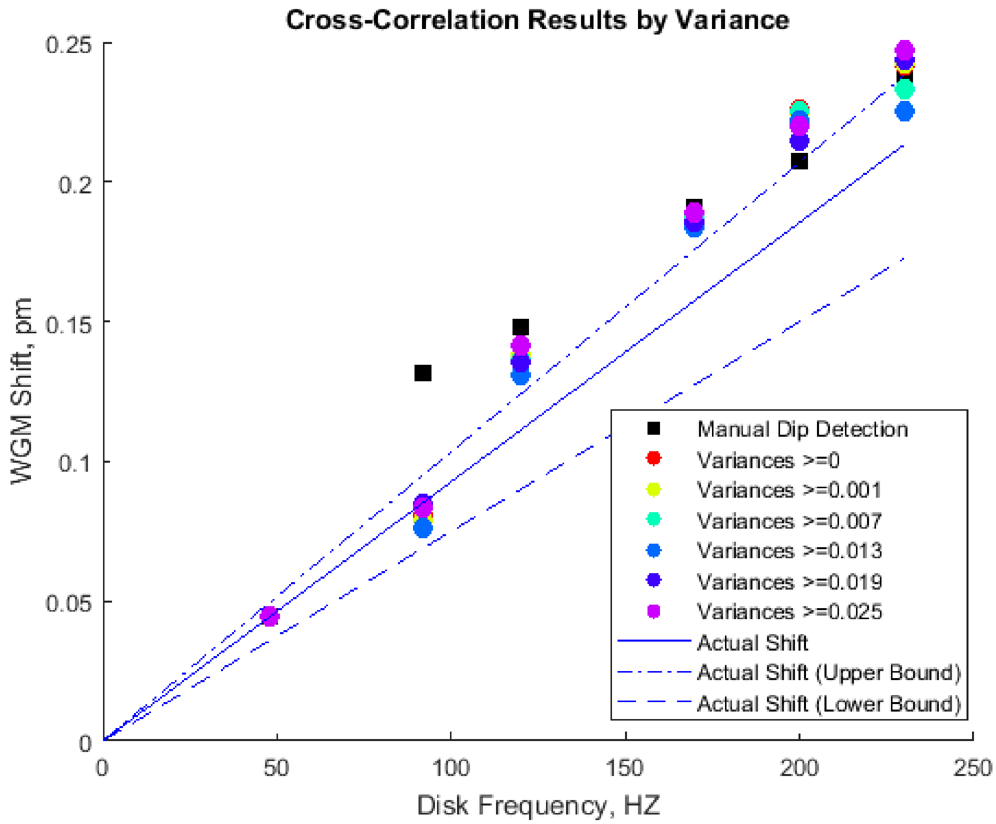

Figure 5.7. WGM Shift vs. Disk Frequency for Manual Dip Detection and Cross-Correlation (for Various Variance Filtering Thresholds)

to note that they are significantly smaller than the enclosed angle of the cone of light being collected by the collection optics and therefore are fairly conservative values.

It is important to make a special note of the data shown at 48 Hz, as Figure 5.7 may otherwise be misleading. Unfortunately, we were unable to make any measurements of the stationary disk which we were able to correlate with the moving measurements due to the intermittent and sensitive nature of the disk coupling. Cross-correlation, as is evident from Equation 5.1, is only able to determine relative shifts between two data vectors. Ordinarily, this would not have been an issue, however, without a zero speed reference to compare it to, the shift between 0Hz and 48Hz cannot be determined. To be most strictly accurate, the point at 48Hz can be taken to be a new origin of the graph, with new axes drawn through it and shifted correspondingly. However, since the calculated (actual) shift depends on the actual velocity of the target, rather than a relative velocity, this strictly accurate representation would have prevented the comparison of the measured shift to the actual shift. Therefore an assumption was made: The cross-correlation results were shifted such that each scan's 48Hz data point corresponded to the 48Hz calculated shift of approximately $0.05pm$. With the assumption that the calculated and the measured shifts would coincide at this first location, it is possible to analyze the shifts in velocity that are measured and compare them to the true value of the shift.

Given this assumption, it is clear that there is good agreement between the predicted and the measured whispering gallery mode shift over the range of disk frequencies, although in general, the measurements slightly, but consistently, over-estimate the value obtained directly from the disk rotational speed. Furthermore, the variance filtered results significantly outperform the manual dip detection method at all but one velocity. As we saw previously, certain intermediate variance filtering cut-off thresholds, specifically the threshold of 0.013, seem to outperform the others and represent an optimum filtering threshold.

$$RMSD = \sqrt{\frac{\sum_{i=1}^{n}(\hat{y}_i - y_i)^2}{N}} \tag{5.3}$$

In order to best quantify the improvement of the variance filtering method over manual dip detection, the root-mean-square-deviation with respect to the calculated shift value, Equation 5.3, was calculated for a large number of variance thresholds (in increments of 0.0001 between variance thresholds of 0.0 and 0.05) and the MDD results. Figure 5.8 shows these results. There are two important conclusions that can be drawn from this figure: Firstly, the fact that the cross-correlation results outperform the manual dip detection results, both for the no variance case filtering (variance threshold = 0.0) and over a range of variance filtering threshold gives significant credence to this application of the algorithm, even under fairly poor coupling conditions and with intermittent signals. Secondly, the fact that the minimum error occurred at a value less than the no variance filtering error indicates

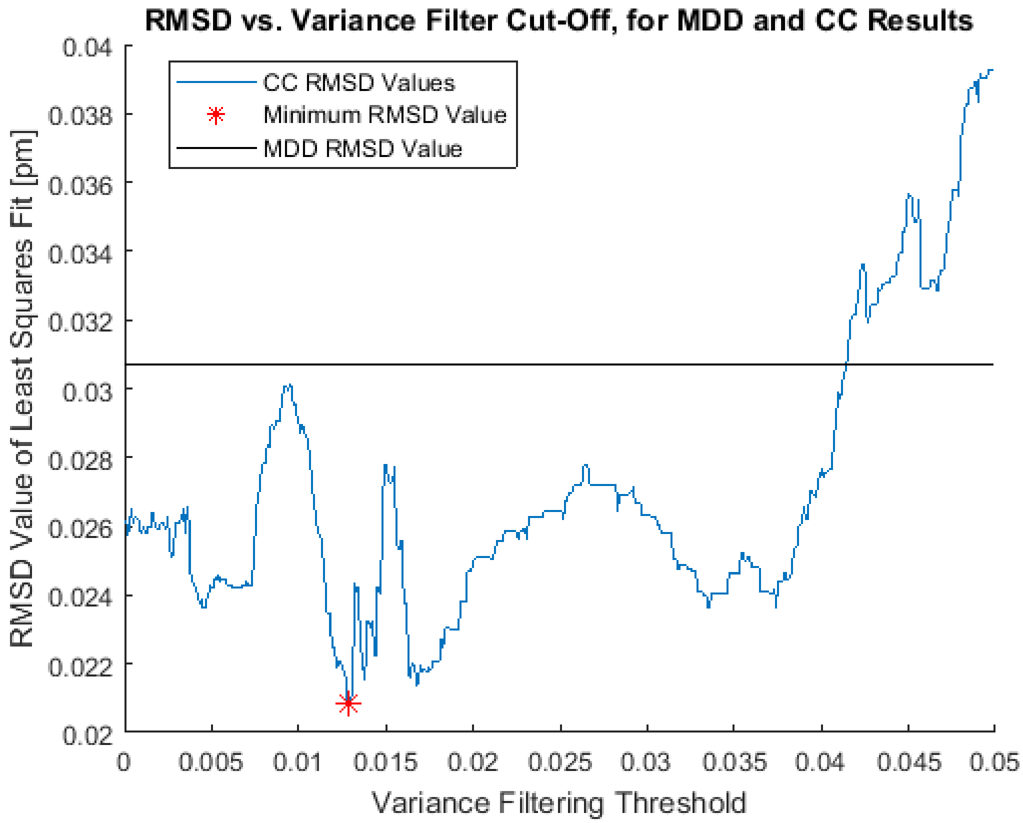

Figure 5.8. Cross-Correlation Best Fit Root-Mean-Square-Deviation for a Range of Variance Thresholds and Manual Dip Detection Results

that not only does variance filtering improve the cross-correlation strength, it also reduces the overall error of the system. We were also able to quantify this error to a value of $0.021pm$ approximately 20% less than the un-filtered error of $0.026pm$ and approximately 30% less than the MDD error of $0.031pm$. Finally, the fact that RMSD values for the variance filtering threshold increase as the threshold gets very large indicates that a high number of scans, i.e. a long integration time or, correspondingly, a higher laser power with a higher scanning rate, is necessary for measurement of unstable signals that experience dropout. The mechanism causing the error fluctuations in RMSD throughout the low variance filtering thresholds is unknown at this time and will be investigated in future work.

In this section, we proposed and demonstrated a signal processing approach for an intermittent signal. Although in the present experiments we use scattered light from a wobbling solid disk, it is clear from this intermittent signal that this signal processing algorithm can be effectively used for Doppler shift in the actual speed sensor (for example, for improving Mie scattered signals). The approach used here is not only effective, but is also a low computational cost approach. Optimization of this filtering method showed that there are two competing effects in minimizing the error. This signal processing method shows significant potential for reducing the error in intermittent signals.

Chapter 6

CONCLUSION

In this thesis, a laser velocity sensor concept based on optical microresonators was presented and its efficacy for and application to spacecraft atmospheric entry was explored. The WGM-based optical microresonators replace the typical Fabry-Perot interferometer and CCD camera system in a single-beam laser velocimetry device, thereby significantly reducing the size and weight of the overall detection system. In the final application, scattering from atmospheric particulates and gas molecules is anticipated. The current state of the art in velocity sensing and LIDAR technologies make the case for the need for a WGM-based velocimeter solution. The preliminary sensor designs and the theory of operation of these sensors indicate that high accuracy velocity sensing with a large dynamic range and small physical size and weight are feasible.

Various tuning methodologies were explored and the results were encouraging. Initial experiments using a piezo-stack to tune the microresonators were encouraging for this velocimetry concept, however limited time-resolution of this approach led us to explore a laser tuned approach as well. Doppler shift detection was satisfactorily demonstrated by observing the whispering gallery optical modes (WGM) of a dielectric microresonator excited by the back scattered light from a solid rotating target using a laser-tuned approach. Two different sensor coupling designs and two measurement methodologies were explored. First, the measurement of Doppler-shift of laser light scattered from a moving target using a dielectric microresonator was shown using side-coupling to a single mode optical fiber. This approach proved to be difficult as beam steering and subsequent signal dropout were experienced. Since the anticipated application requires scattering from atmospheric particles, signal dropout and beam steering are expected to be part of the final application. Ensemble averaging of the signal showed promise in compensating for these difficulties, however, the light level loss of $\sim 99.63\%$ between collection aperture (the total usable scattered photon flux) and photodetector (usable measurement photon flux) will need to be reduced in order to make this method viable. Another approach to mitigate signal dropout due to beam steering was direct free-space coupling of scattered light into the optical resonator and observing the WGMs in the light scattered from the resonator surface. This approach was successful and simulated Doppler shift detection was demonstrated.

In the fiber-coupled rotating-disk experiment, using a microresonator with a Q-factor of $\sim 6\times10^6$, and using the cross-correlation algorithm, an estimate for the minimum wavelength resolution was determined. Current estimates for wavelength resolution of this system are on the order of $\sim 10fm$. In a full, or nearly full, backscatter configuration, this result indicates that, for a full back-scatter single-beam LIDAR system a velocity resolution of $\sim 2.4m/s$ is possible.

The need for a computationally efficient signal processing approach was clearly demonstrated by the experimental results. A data analysis algorithm was introduced and tested to improve the determination of WGM shifts by increasing cross-correlation strength when the signal-to-noise ratio is limited. We showed that a signal processing algorithm that only selects scans with variances over a certain threshold value can help to mitigate the signal dropout effects. The low computational complexity and effectiveness of this approach were also demonstrated.

In this thesis, the groundwork for a WGM-based optical Doppler velocimeter was demonstrated via proof-of-concept experiments and a low-computational complexity signal processing approach. However, the added difficulty in making measurements from a stream of fast moving particles is clearly the next big challenge in demonstrating the viability of this system. After demonstrating this sensor design in measuring the velocity of a stream of particles at the proof-of-concept level, detection can be optimized and the signal processing approaches can be integrated with the pre-existing software. Additional research into unexpected behavior of the variance filtering approach must also take place.

The results presented in this thesis are very encouraging. The ability to accurately and directly detect velocity changes during entry, descent, and landing operations will be a significant advantage in spaceflight. With the development of sensors such as this one, disasters such as the Schiaparelli lander crash will perhaps become avoidable and the enhanced operational security, provided by sensors such as this one, will be instrumental in paving the way to human spaceflight to places in the solar system previously unreachable to mankind.

BIBLIOGRAPHY

[1] Ali, A. R. *Dielectric Micro-Resonator-Based Opto-Mechanical Systems for Sensing Applications*. PhD thesis, Southern Methodist University, 2015. vii, 15, 28, 47, 54

[2] Arnold, S., Khoshsima, M., Teraoka, I., Holler, S., and Vollmer, F. Shift of Whispering-Gallery Modes in Microspheres by Protein Adsorption. *Opt. Lett. 28*, 4 (Feb 2003), 272–274. 7

[3] Arnold, S., and Shopova, S. I. *Whispering Gallery Mode Biosensor*. Springer Netherlands, Dordrecht, 2011, pp. 237–259. 7

[4] Ayaz, U. K., Ioppolo, T., and Otugen, M. V. Wall Shear Stress Sensor Based on the Optical Resonances of Dielectric Microspheres. *Measurement Science and Technology 22*, 7 (2011), 075203. 7

[5] Blair, S., and Chen, Y. Resonant-Enhanced Evanescent-Wave Fluorescence Biosensing with Cylindrical Optical Cavities. *Appl. Opt. 40*, 4 (Feb 2001), 570–582. 7

[6] Borselli, M., Srinivasan, K., Barclay, P. E., and Painter, O. Rayleigh Scattering, Mode Coupling, and Optical Loss in Silicon Microdisks. *Applied Physics Letters 85*, 17 (2004), 3693–3695. 16

[7] Campbell, M., Cosgrove, J., Greated, C., Jack, S., and Rockliff, D. Review of LDA and PIV Applied to the Measurement of Sound and Acoustic Streaming. *Optics and Laser Technology 32*, 7 (2000), 629 – 639. Optical methods in heat and fluid flow. 4

[8] Cao, X., Liu, J., Jiang, N., and Chen, Q. Particle Image Velocimetry Measurement of Indoor Airflow Field: A Review of the Technologies and Applications. *Energy and Buildings 69* (2014), 367 – 380. 4

[9] ESA Inspector General Tolker-Nielsen, T. EXOMARS 2016 - Schiaparelli Anomaly Inquiry. Tech. rep., European Space Agency, 2017. 2

[10] Fourguette, D., Otugen, M., Larocque, L., Ritter, G., Meeusen, J., and Ioppolo, T. Whispering-Gallery-Mode-Based Seismometer, June 3 2014. US Patent 8,743,372. 7, 41

[11] Grudinin, I. S., Ilchenko, V. S., and Maleki, L. Ultrahigh Optical Q Factors of Crystalline Resonators in the Linear Regime. *Phys. Rev. A 74* (Dec 2006), 063806. 17

[12] Guan, G., Arnold, S., and Otugen, V. Temperature Measurements Using a Microoptical Sensor Based on Whispering Gallery Modes. *AIAA Journal 44*, 10 (Oct 2006), 2385–2389. 7

[13] Hegarty, C. J., and Chatre, E. Evolution of the Global Navigation Satellite System (GNSS). *Proceedings of the IEEE 96*, 12 (Dec 2008), 1902–1917. 3

[14] Ioppolo, T., Ayaz, U., and Otugen, M. V. Tuning of Whispering Gallery Modes of Spherical Resonators Using an External Electric Field. *Optics Express 17*, 19 (Jan 2009), 16465. 7, 41

[15] Ioppolo, T., Das, N., and Otugen, M. V. Whispering Gallery Modes of Microspheres in the Presence of a Changing Surrounding Medium: A New Ray-Tracing Analysis and Sensor Experiment. *Journal of Applied Physics 107*, 10 (2010), 103105. 7, 13, 18

[16] Ioppolo, T., Kozhevnikov, M., Stepaniuk, V., Otugen, M. V., and Sheverev, V. Micro-Optical Force Sensor Concept Based on Whispering Gallery Mode Resonators. *Applied Optics 47*, 16 (2008), 3009. 7, 17

[17] Ioppolo, T., and Otugen, M. V. Pressure Tuning of Whispering Gallery Mode Resonators. *J. Opt. Soc. Am. B 24*, 10 (Oct 2007), 2721–2726. 7

[18] Ioppolo, T., and Otugen, M. V. Magnetorheological Polydimethylsiloxane Micro-optical Resonator. *Opt. Lett. 35*, 12 (Jun 2010), 2037–2039. 7

[19] Ioppolo, T., Otugen, M. V., and Marcis, K. Magnetic Field-Induced Excitation and Optical Detection of Mechanical Modes of Microspheres. *Journal of Applied Physics 107*, 12 (2010), 123115. 7

[20] LaPenna,Vincent G. *Automated Tracking of Optical Resonance Shifts of Dielectric Micro-Resonators*. PhD thesis, 2013. Copyright - Database copyright ProQuest LLC; ProQuest does not claim copyright in the individual underlying works; Last updated - 2016-03-09. 54

[21] Lord Rayleigh, O.M., F.R.S. CXII. The Problem of the Whispering Gallery. *The London, Edinburgh, and Dublin Philosophical Magazine and Journal of Science 20*, 120 (1910), 1001–1004. 12

[22] Matsko, A., and Ilchenko, V. Optical Resonators with Whispering-Gallery Modes-Part I: Basics. *IEEE Journal of Selected Topics in Quantum Electronics: A Publication of the IEEE Lasers and Electro-Optics Society 12*, 3 (2006), 3–14. 1, 13

[23] Matsko, A. B., Savchenkov, A. A., Strekalov, D., Ilchenko, V. S., and Maleki, L. Review of Applications of Whispering-Gallery Mode Resonators in Photonics and Nonlinear Optics. Tech. Rep. 42-162, National Aeronautics and Space Administration: Jet Propulsion Laboratory, 2005. 6

[24] Matsubara, K., Stork, W., Wagner, A., Drescher, J., and Müller-Glaser, K. D. Simultaneous Measurement of the Velocity and the Displacement of the Moving Rough Surface by a Laser Doppler Velocimeter. *Appl. Opt. 36*, 19 (Jul 1997), 4516–4520. 5

[25] Michigan Aerospace Corporation. AeroForecast®Optical Air Data System, 2017. 2

[26] National Instruments Corporation. NI 6115/6120 Specifications, Sep 2008. http://www.ni.com/pdf/manuals/371397c.pdf. 28

[27] New Focus. Model TLB-6800 Vortex Plus™Laser System, 2014. 25

[28] Nguyen, N. Q., Gupta, N., Ioppolo, T., and Ötügen, M. V. Whispering Gallery Mode-based Micro-Optical Sensors for Structural Health Monitoring of Composite Materials. *Journal of Materials Science 44*, 6 (Mar 2009), 1560–1571. 7

[29] Otugen, M. V., Su, W.-J., and Papadopoulos, G. A New Laser-Based Method for Strain Rate and Vorticity Measurements. *Measurement Science and Technology 9*, 2 (1998), 267. 24

[30] Savchenkov, A. A., Matsko, A. B., Ilchenko, V. S., and Maleki, L. Optical Resonators with Ten Million Finesse. *Opt. Express 15*, 11 (May 2007), 6768–6773. 17

[31] SBIR/STTR Program Office and Fourguette, Dominique and Dodds, John A. NASA SBIR 2016 Solicitation: 16-2 S4.01-7996. *NASA SBIR 2016 Solicitation: 16-2 S4.01-7996* (Jul 2017). Only Abstract and Proposal Summary Available Online. Full proposal not published online. vii, 8, 9, 10

[32] Scientific and Technical Information Office and Gracey, W. *Measurement of Aircraft Speed and Altitude*. National Aeronautics and Space Administration, Scientific and Technical Information Office, 1980. 3

[33] ThorLabs. 150V USB Closed-Loop Piezo Controllers. 27

[34] ThorLabs. Piezoelectric Actuators with Attached Strain Gauges. 27

[35] ThorLabs. Single Mode Fiber - SM600, Jan 2015. 35

[36] ThorLabs, Inc. Piezoelectric Tutorial: Introduction. https://www.thorlabs.com/newgrouppage9.cfm?objectgroup˙id=5030. vii, 19

[37] Truax, B. E., Demarest, F. C., and Sommargren, G. E. Laser Doppler Velocimeter for Velocity and Length Measurements of Moving Surfaces. *Appl. Opt. 23*, 1 (Jan 1984), 67–73. 5

[38] User: Cmglee. *Comparison of Convolution and Correlation*. Wikimedia Commons. This file is licensed under the Creative Commons Attribution-Share Alike 3.0 Unported license. https://creativecommons.org/licenses/by-sa/3.0/deed.en. It was modified by Benjamin Wise to omit the convolution column. viii, 46

[39] User: Femtoquake. *St Paul's Cathedral Whispering Gallery*. Wikimedia Commons. This file is licensed under the Creative Commons Attribution-Share Alike 3.0 Unported license. https://creativecommons.org/licenses/by-sa/3.0/deed.en. vii, 11

[40] Vollmer, F., and Arnold, S. Whispering-Gallery-Mode Biosensing: Label-Free Detection Down to Single Molecules. *Nature Methods 5* (Jun 2008), 591 EP –. Perspective. 7

[41] Vollmer, F., Braun, D., Libchaber, A., Khoshsima, M., Teraoka, I., and Arnold, S. Protein Detection by Optical Shift of a Resonant Microcavity. *Applied Physics Letters 80*, 21 (2002), 4057–4059. 7

[42] Wise, B. J., Eghbalifarkoosh, V., Otugen, V., and Fourguette, D. A Microresonator Based Laser Velocity Sensor. *2018 AIAA Aerospace Sciences Meeting, AIAA SciTech Forum* (Jan 2018). 7